Master of Science in Applied Geophysics

Research Thesis

Marine Unexploded Ordnance Detection with the Transient Electromagnetic Method

A Numerical Feasibility Study

Jan Willem Buist

August 21, 2020

IDEA League

Marine Unexploded Ordnance Detection with the Transient Electromagnetic Method

A Numerical Feasibility Study

Master of Science Thesis

for the degree of Master of Science in Applied Geophysics at
Delft University of Technology
ETH Zürich
RWTH Aachen University
by

Jan Willem Buist

August 21, 2020

Department of Geoscience & Engineering · Delft University of Technology
Department of Earth Sciences · ETH Zürich
Faculty of Georesources and Material Engineering · RWTH Aachen University

Printed in The Netherlands

IDEA LEAGUE
JOINT MASTER'S IN APPLIED GEOPHYSICS

Delft University of Technology, The Netherlands
ETH Zürich, Switzerland
RWTH Aachen, Germany

Dated: *August 21, 2020*

Committee Members:

Prof. Dr. Ir. Evert C. Slob

Dr. Norbert Klitzsch

Dr. Ir. Dieter Werthmüller

Dr. Johannes M. Singer

Dr. Vsevolod Kovalenko

Dr. Ir. Deyan Draganov

Supervisors:

Prof. Dr. Ir. Evert C. Slob

Dr. Ir. Dieter Werthmüller

Dr. Johannes M. Singer

Dr. Vsevolod Kovalenko

Abstract

The hazards of unexploded ordnance threaten the increasing marine construction activities nowadays, which increases the importance of unexploded ordnance detection. Research has shown that transient electromagnetic methods can successfully be used to detect unexploded ordnance on land. New equipment is being developed to make marine unexploded ordnance detection also possible. This study aims to determine which targets can be detected and which not in a marine environment through a numerical feasibility study. Building on an existing geophysical simulation framework, it asks: Under which conditions can we detect a conductor on or below the seafloor using a time domain loop source? Through the three-dimensional modelling of Maxwell's equations, responses were computed for hollow rectangular targets of different burial depths, sizes, wall thicknesses, and wall conductivities. For the analysis of these responses two quantities were introduced, a net effect and a measurability. Evaluation of these quantities demonstrated the individual impact of the tested parameters on these quantities as well as the relative significance of the influence of these parameters. The results included derived relations for the influence of individual parameters on the net effect, as well as limits on the measurability of targets. A rectangular conductor of 0.1 by 0.1 by 0.4 metres or smaller with a wall thickness of 10 millimetre, buried more than 2 metres under the seafloor is not measurable under the noise assumptions made. The relative significance of the parameters was found to be from most to least significant: burial depth, size, wall conductivity, and wall thickness.

Acknowledgements

First of all I would like to extend my deepest gratitude towards my supervisors Evert Slob, Dieter Werthmüller, Johannes Singer and Vsevolod Kovalenko. Through our fruitful Skype conversations they pointed me in the right direction and gave me valuable insights into both the theoretical and practical aspects of my subject.

I am also grateful to all my friends who supported me throughout my studies in Delft, Zürich, and Aachen. Pursuing this Master's degree would not be so enjoyable without my classmates. Special thanks goes to James Russell, who learned me some proper English and how to brew a pot of tea. And to my roommates, with whom I spent this period in our house/office.

I would like to thank my family. I very much appreciate the unconditional support from my parents, grandparents, and sisters. They always encouraged me with their profound belief of my abilities. Last but not least, I would like to thank Laurien for everything.

Jan Willem Buist
Delft, August 2020

Contents

List of Figures

List of Tables

Notation and conventions

Symbols

Symbol	Description	Units
A	Area	m^2
E_p	Relative error	$\%$
H	Target height	m
I	Current	A
L	Target length	m
S_c	Characteristic size	m
W	Target width	m
Δx_{wall}	Target wall thickness	m
δ	Skin depth	m
ϵ	Electrical permittivity	$\mathrm{F/m}$
$\mathbf{b}$	Magnetic flux density	T
$\mathbf{d}$	Electric displacement	$\mathrm{C/m}^2$
$\mathbf{e}$	Electric field	$\mathrm{V/m}$
$\mathbf{h}$	Magnetic field	$\mathrm{A/m}$
$\mathbf{j}$	Free current density	$\mathrm{A/m}^2$
$\mathcal{M}$	Measurability	
$\mathcal{N}$	Net effect	
μ	Magnetic permeability	$\mathrm{H/m}$
π	The ratio of a circle's circumference to its diameter	
ρ	Resistivity	$\Omega\,\mathrm{m}$
σ	Conductivity	$\mathrm{S/m}$
τ	Magnetic dipole moment	$\mathrm{A\,m}^2$
ϱ	Electric charge density	$\mathrm{C/m}^3$
d	Depth	m
f	Placeholder for any function	
p	Placeholder for any probability density function	
t	Time	s

Acronyms

CDF Cumulative Distribution Function.

CSEM Controlled Source Electromagnetic.

EM ElectroMagnetic.

EMI Electromagnetic Induction.

ERW Explosive Remnants of War.

FDEM Frequency Domain Electromagnetics.

GPR Ground Penetrating Radar.

HE High Explosive.

MT MagnetoTelluric.

NRMSE Normalised Root Mean Square Error.

NSEM Natural Source Electromagnetic.

PDF Probability Density Function.

RMSE Root Mean Square Error.

TDEM Time Domain Electromagnetics.

TEM Transient Electromagnetic.

tTEM Towed Transient Electromagnetic.

UXO Unexploded Ordnance.

VTI Vertical Transverse Isotropy.

ZTEM Z-axis tipper Electromagnetics.

Software

custEM Customizable Electromagnetic Modeling,
Reference: Rochlitz, Skibbe, and Günther (2019),
Website: `custem.readthedocs.io`.

emg3d Multigrid solver for 3D EM diffusion,
Reference: Werthmüller, Mulder, and Slob (2019),
Website: `empymod.github.io`.

EMmod ElectroMagnetic Modelling,
Reference: Hunziker, Thorbecke, and Slob (2015),
Website: `software.seg.org/2015/0001`.

empymod 3D EM modeller for 1D VTI media,
Reference: Werthmüller (2017),
Website: `empymod.github.io`.

PETGEM Parallel Edge-based Tool for Geophysical Electromagnetic Modelling,
Reference: Castillo-Reyes, de la Puente, and Cela (2018),
Website: `petgem.bsc.es`.

SimPEG Simulation and Parameter Estimation in Geophysics,
Reference: Cockett, Kang, Heagy, Pidlisecky, and Oldenburg (2015),
Website: `simpeg.xyz`.

1 | Introduction

In many periods throughout human history, mankind has fought wars with each other. Over time, the preferred tool in those wars evolved from swords to all kinds of explosive weapons. Nowadays, problems arise with explosives that did not detonate. All types of explosives together (bombs, shells, grenades, mines, et cetera) which did not detonate during combat or were disposed are called Unexploded Ordnance (UXO) or Explosive Remnants of War (ERW). In this thesis they are addressed as UXO. All over the world, the risk of a UXO detonating can have serious implications and be a potential threat. Between 1999 and 2019 the mean yearly death rate due to UXO detonation was at least above 6000 people worldwide. Since 1999, the yearly casualties are monitored by the International Campaign to Ban Landmines – Cluster Munition Coalition. Their data is given in Figure 1.1. (*Landmine Monitor 2019: 21st annual edition*, 2019)

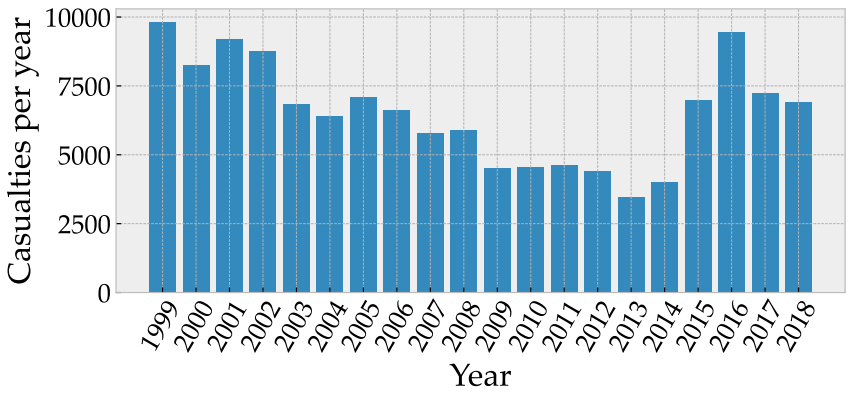

Figure 1.1: Confirmed UXO casualties annually (1999-2018), adapted from *Landmine Monitor 2019: 21st annual edition* (2019).

Not only on land, but also in the marine environment there are many areas contaminated with UXO. Offshore ammunition dump sites, naval mine fields, and naval battles are three main sources of marine UXO. The marine environment is changing constantly due to tidal effects and UXO locations are changing with it. In these times, where the number of marine structures, such as wind turbines and oil platforms, is increasing rapidly, the need for marine UXO detection grows with it.

1.1 Review

Various geophysical techniques are applied to detect UXO. The most frequently used techniques are Electromagnetic Induction (EMI) and magnetometry (Zhang, Collins, Yu, Baum, & Carin, 2003). Magnetometry is applied for UXO detection both on land (Billings, 2004) and in marine settings (Salem, Hamada, Asahina, & Ushijima, 2005). In magnetometry surveys, local distortions in the Earth's magnetic field are measured. The distortions can be caused by ferrous objects or minerals. In general, magnetometry measurements are done in the far field of the target and therefore usually only recover the dipole moment of a target. Classification of the objects size and shape from only the dipole moment involves a lot of uncertainty and therefore determining UXO size with magnetometry is difficult. Furthermore, magnetometry is not susceptible for non-ferrous targets, such as aluminium (Billings, 2004).

The other main technique, EMI, uses a time varying primary magnetic field which induces eddy currents in conductive targets. The eddy currents produce a secondary magnetic field which is measured by the receiver. The secondary field can be measured alone in so-called Time Domain Electromagnetics (TDEM) methods or along with the primary field in so-called Frequency Domain Electromagnetics (FDEM) methods. The time domain methods make use of a finite pulse primary field. After the shutdown of the primary field, the induced secondary field is measured. The rate of decay contains the information about the subsurface properties. Frequency domain methods make use of a periodic continuous signal, which is constantly measured by the receiver. Here, the received signal's amplitude and phase provide the useful information (Pasion, 2007). In the world of geophysical ElectroMagnetic (EM) methods, terminology and abbreviations may cause confusion. In principle, all active methods are called Controlled Source Electromagnetic (CSEM) methods and all passive methods are called Natural Source Electromagnetic (NSEM) methods. Common passive methods are MagnetoTelluric (MT) and Z-axis tipper Electromagnetics (ZTEM). Active methods can be subdivided into time domain methods (TDEM or Transient Electromagnetic (TEM)) and frequency domain methods (FDEM). In practice, some acronyms are used for fewer methods then they actually include. The acronym CSEM is used primarily for an offshore FDEM method to explore for horizontally large resistive bodies. Time domain methods using a loop source are frequently called TEM in practice. Both frequency domain methods (Zhang et al., 2003) and time domain methods (Pasion & Oldenburg, 2001) are used to detect UXO.

To a lesser extent, Ground Penetrating Radar (GPR) has been used for UXO detection (Sato, Fujiwara, Feng, Zhou, & Kobayashi, 2005), although it is negatively influenced by wave attenuation in the ground and therefore strongly limited in sensing deeply buried UXO (Zhang et al., 2003).

Recently, studies have been conducted on using TEM for UXO detection (Shubitidze et al., 2013; Doll et al., 2010) and new equipment has been especially built for these investigations (MacInnes, Snyder, & Zonge, 2002; Prouty, George, & Snyder, 2011). Multi-component receivers are being used to generate high density data and make a possible inversion for parameters easier. There is, however, little known of which targets these sensors can measure and which targets they cannot.

To compute how these new sensors would respond to different types of UXO, there are two main approaches possible. The first approach is approximating UXO targets with dipole models and computing TEM responses from the dipole model (Pasion & Oldenburg, 2001). The second approach is to simulate the whole survey by numerically modelling Maxwell's equations. This approach yields a more precise result although at a much greater computational cost.

For one-dimensional problems, Maxwell's equations can be modelled in semi-analytic fashion. The package empymod (Werthmüller, 2017) can compute electric and magnetic responses for layered earth models with Vertical Transverse Isotropy (VTI). It models Maxwell's equations in three-dimensional space for one-dimensional models. It is based on EMmod from Hunziker et al. (2015) and uses the Fourier and Hankel transforms from Key (2012). Realistic simulations require three-dimensional models as an input. Various software packages for the three-dimensional modelling of Maxwell's equations exist that accept three-dimensional models. Four open-source ones are: custEM (Rochlitz et al., 2019), emg3d (Werthmüller et al., 2019), PETGEM (Castillo-Reyes et al., 2018), and SimPEG (Cockett et al., 2015). These four packages have in common that they solve the formulation of Maxwell's equations under the diffusive approximation. The packages emg3d and SimPEG use the finite volume method on structured grids. The other two, custEM and PETGEM, use the finite element method on unstructured tetrahedral meshes. For applications in the TEM field, the SimPEG package is the most advanced.

1.2 Contribution

This research is focused on the shallow marine environment (i.e. seas on the continental shelf). In this environment we explore the TEM responses of different objects on or below the seafloor. For simplicity, all objects are rectangular. We acquire these responses through three-dimensional modelling of Maxwell's equations. The difference between these objects can be in the size and shape, orientation, or physical properties of the object.

We carry out our research under the main question of interest: ***Under which conditions can we detect a conductor on the seafloor using a time domain loop source?*** To answer this question, we first have to find a measurable signal. To quantify how measurable a single signal is, we introduce the *net effect* and the *measurability*. These quantities give a number to each signal, which makes comparisons between different signals more straightforward.

The conditions we focus on in our research are those of the conductor. The actual classifier, a device that will tell if a measurable signal is or is not a target of interest, is out of scope of our investigation. The conditions of the source and receiver instruments are also out of our research scope and therefore we keep them simple.

In our research, we mainly use SimPEG. From the available open-source options, it is the most advanced regarding time-domain computations. Next to SimPEG we use empymod to create semi-analytical background signals. We limit ourselves to using the SimPEG framework for our simulations. Through the forward modelling simulations, we investigate how each individual

parameter influences the measurability and in addition we compare the influences of the different parameters.

The goals of our research are summarised by the main question and underlying sub questions:

- Under which conditions can we detect a conductor on or below the seafloor using a time domain loop source?
  - How can we define the measurability of sensing on a target?
  - How accurately can we solve TDEM problems with SimPEG?
  - What is the influence of the individual parameters on the measurability?
  - What is the relative significance of the influence of different parameters on the measurability?

1.3 Outline of this thesis

In order to answer the research questions posed above this thesis is written in the following way. This introductory chapter is followed by a description of the necessary theory underlying the electromagnetic measurements and the of the common UXO types relevant for this study in Chapter 2. Chapter 3 describes the validation of the SimPEG software. Subsequently, we define our approach to answer the main research question in Chapter 4. After that we give the results and discussion of our study in Chapter 5. Finally we conclude our research in Chapter 6.

2 | Background

In this chapter, we review the relevant background literature for our research. First we dive into the relevant physics starting with Maxwell's equations. Then we discuss the physical properties which influence CSEM methods. Hereafter, we examine the noise in CSEM methods. Finally, we give an overview of common found UXO types.

2.1 Maxwell's equations

All CSEM methods make use of electromagnetism. How the electromagnetic field behaves is described by Maxwell's equations. Maxwell's equations in differential form in the time domain are given in Equation 2.1 to Equation 2.4. (Lorrain & Corson, 1970). These equations contain six different vector functions $\mathbf{b}$, $\mathbf{d}$, $\mathbf{e}$, $\mathbf{h}$, $\mathbf{j}$, $\mathbf{j^m}$, and $\mathbf{j^e}$, with:

$\mathbf{b}$: magnetic flux density (in T or $\mathrm{Wb/m^2}$)
$\mathbf{d}$: electric displacement (in $\mathrm{C/m^2}$)
$\mathbf{e}$: electric field (in $\mathrm{V/m}$)
$\mathbf{h}$: magnetic field (in $\mathrm{A/m}$)
$\mathbf{j}$: volumetric density of induced current (in $\mathrm{A/m^2}$)
$\mathbf{j^m}$: volumetric density of external magnetic current (in $\mathrm{A/m^2}$)
$\mathbf{j^e}$: volumetric density of external electrical current (in $\mathrm{A/m^2}$)

The other parameter in this set of differential equations is ϱ for the electric charge density. Maxwell's equations are given by:

$$\nabla \cdot \mathbf{d} = \varrho, \qquad \text{(Gauss's law)} \tag{2.1}$$

$$\nabla \cdot \mathbf{b} = 0, \qquad \text{(Gauss's law for magnetism)} \tag{2.2}$$

$$\nabla \times \mathbf{e} + \frac{\partial \mathbf{b}}{\partial t} = -\mathbf{j^m}, \qquad \text{(Faraday's law)} \tag{2.3}$$

$$-\nabla \times \mathbf{h} + \frac{\partial \mathbf{d}}{\partial t} + \mathbf{j} = -\mathbf{j^e}. \qquad \text{(Ampère's law with Maxwell's addition)} \tag{2.4}$$

Specific formulations of Maxwell's equations can be acquired through the constitutive relations. The constitutive relations in the frequency domain are given in Equation 2.5 to Equation 2.7, where $\mathbf{B}, \mathbf{D}, \mathbf{E}, \mathbf{H}$, and $\mathbf{J}$ are the frequency domain versions of $\mathbf{b}, \mathbf{d}, \mathbf{e}, \mathbf{h}$, and $\mathbf{j}$, ϵ is the electrical permittivity, μ is the magnetic permeability, and σ the electrical conductivity. In these equations

it is already assumed that all media are linear, isotropic, homogeneous, and possess electrical properties which are independent of time, temperature, and pressure. (Nabighian, 1991)

$$\mathbf{B} = \mu(\omega)\mathbf{H}, \tag{2.5}$$
$$\mathbf{D} = \epsilon(\omega)\mathbf{E}, \tag{2.6}$$
$$\mathbf{J} = \sigma(\omega)\mathbf{E}. \tag{2.7}$$

The time domain equivalent of these equations can be obtained by taking the inverse Fourier transform of each, yielding:

$$\mathbf{b} = \mu(t) * \mathbf{h}, \tag{2.8}$$
$$\mathbf{d} = \epsilon(t) * \mathbf{e}, \tag{2.9}$$
$$\mathbf{j} = \sigma(t) * \mathbf{e}. \tag{2.10}$$

If the medium is instantaneously reacting the constitutive relations in the time domain simplify to:

$$\mathbf{b} = \mu\mathbf{h}, \tag{2.11}$$
$$\mathbf{d} = \epsilon\mathbf{e}, \tag{2.12}$$
$$\mathbf{j} = \sigma\mathbf{e}. \tag{2.13}$$

In CSEM applications the influence of electrical permittivity is negligible. This is called the diffusive approximation. This can be showed with the charge conservation law:

$$\frac{\partial \varrho}{\partial t} = -\nabla \cdot (\mathbf{j} + \mathbf{j}^{\mathbf{e}}). \tag{2.14}$$

When an initial charge distribution ϱ_0 is released at $t = 0\text{s}$ in a source-free region, Ziolkowski and Slob (2019) find the following equation from the charge conservation law:

$$\frac{\partial \varrho}{\partial t} = -\frac{\partial \sigma}{\partial \epsilon}\varrho. \tag{2.15}$$

This first order differential equation has the following solution:

$$\varrho(t) = \varrho_0 \exp(-\sigma t/\epsilon). \tag{2.16}$$

In the exponent of this function, the inverse of the ratio ϵ/σ can be found. This ratio is called the charge relaxation time and is a measure of the time it takes for a medium disturbed by a passing electromagnetic field to return to its equilibrium. If the time variation of this passing electromagnetic field is slow compared with the the charge relaxation time, epsilon can be neglected in Maxwell's equations and the diffusive approximation can be made. For most earth materials the relaxation time is less than 10 μs (Ziolkowski & Slob, 2019). This means that for TEM, where usually the first measurement is taken well after 100 μs the diffusive approximation is valid.

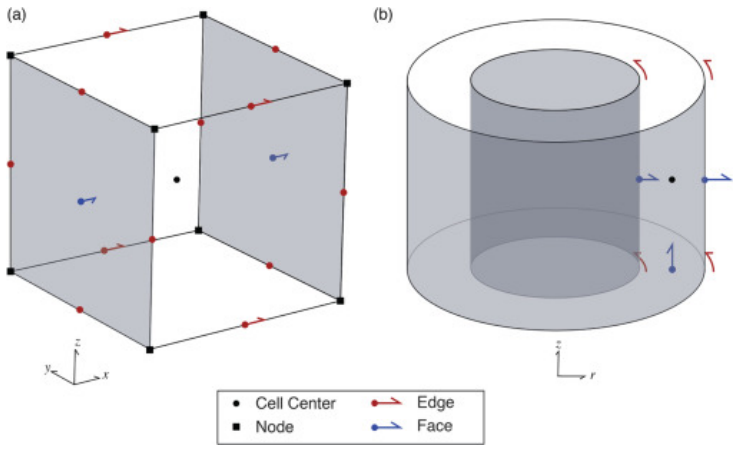

Figure 2.1: Discretisation of a single cell in (a) Cartesian and (b) cylindrical coordinates (Figure 2 from Heagy et al. (2015)). Red arrows represent fields, blue arrows represent fluxes, and black dots represent physical properties.

From Equation 2.3, Equation 2.4, the diffusive approximation, and the constitutive relations for instantaneously reacting media the following relations depending solely on $\mathbf{e}$ or $\mathbf{h}$ can be obtained:

$$\nabla \times \mu^{-1} \nabla \times \mathbf{e} + \sigma \frac{\partial \mathbf{e}}{\partial t} = -\nabla \times \mu^{-1} \mathbf{j}^{\mathbf{m}} - \frac{\partial \mathbf{j}^{\mathbf{e}}}{\partial t}, \tag{2.17}$$

$$\nabla \times \sigma^{-1} \nabla \times \mathbf{h} + \mu \frac{\partial \mathbf{h}}{\partial t} = \nabla \times \sigma^{-1} \mathbf{j}^{\mathbf{e}} - \mathbf{j}^{\mathbf{m}}. \tag{2.18}$$

In Equation 2.17 we end up with the TDEM modelling equation used by SimPEG for the electric field (Heagy, Cockett, Kang, Rosenkjaer, & Oldenburg, 2017). This equation is discretised and solved with a spatial finite element scheme and a backward Euler scheme in time by SimPEG.

The discretisation of Maxwell's equations is done on a staggered mimetic grid, which is described by Hyman and Shashkov (1999) and is based on previous research by Yee (1966). In this discretisation fields are discretised on edges, fluxes on faces, and physical properties at cell centres. The locations of the edges, faces and centres in Cartesian and cylindrical coordinates are given in Figure 2.1, where fields are represented with red arrows, fluxes with blue arrows, and physical properties with black dots.

2.2 Relevant physical properties

Here we discuss the physical properties electrical conductivity (σ) and magnetic permeability (μ). Both of these are used as diagnostic properties in UXO surveys. Their relation to the electric and magnetic field was given in the constitutive relations Equation 2.5 and Equation 2.7.

The values for common UXO materials of both the electrical conductivity and the relative magnetic permeability are given in Table 2.1. In Figure 2.2 typical conductivity values for geological

targets are given. Electrical conductivity and magnetic permeability are explained in more detail below.

Table 2.1: Values of conductivity and relative magnetic permeability for various metals. Adapted from O'Neill (2016).

Material	**Conductivity** $(\mathrm{S/m})$	**Relative magnetic permeability**
Stainless steel	1.5×10^6	1
Aluminium	35×10^6	1
Copper	60×10^6	1
Carbon steel	7×10^6	100

Magnetic permeability

The magnetic permeability (μ) is a property that describes the degree of magnetisation a material under influence of a magnetic field. The degree of magnetisation is how much of induced magnetism a material experiences under the influence of an external magnetic field. From Equation 2.5, we can see the magnetic permeability is the ratio between the magnetic flux density in a material and the magnetic field intensity applied to it.

Although the main effect in the TDEM response is due to eddy currents in conductors, it has been shown that large anomalies in the magnetic permeability can result in measurable anomalous effects to the TDEM response (Pavlov & Zhdanov, 2001). Thus, the magnetic permeability values should also be taken into account when modelling the TDEM surveys for UXO detection.

Often, the magnetic permeability is represented as a relative permeability. The relative permeability, the ratio between the permeability of a specific medium and the permeability of free space is given by:

$$\mu_r = \frac{\mu}{\mu_0}. \tag{2.19}$$

Where μ is the permeability of the material, μ_0 is the permeability of free space or magnetic constant with value $\mu_0 = 4\pi \times 10^{-7}\ \mathrm{H/m}$. Relative magnetic permeabilities for common UXO materials vary from 1 to 100, see Table 2.1.

Electrical conductivity

Electrical conductivity (σ) quantifies to what extent a material is able to induce a current when subjected to an electrical field. Its value in $\mathrm{S/m}$ varies several orders of magnitude for different materials. Typical conductivity values for geological targets are in the range between 0.01 $\mathrm{mS/m}$ and 100 $\mathrm{S/m}$, see Figure 2.2. Values of conductivity for common UXO materials vary from 1.5 to 60 $\mathrm{MS/m}$, see Table 2.1. The reciprocal of electrical conductivity is electrical resistivity (ρ in $\Omega\,\mathrm{m}$).

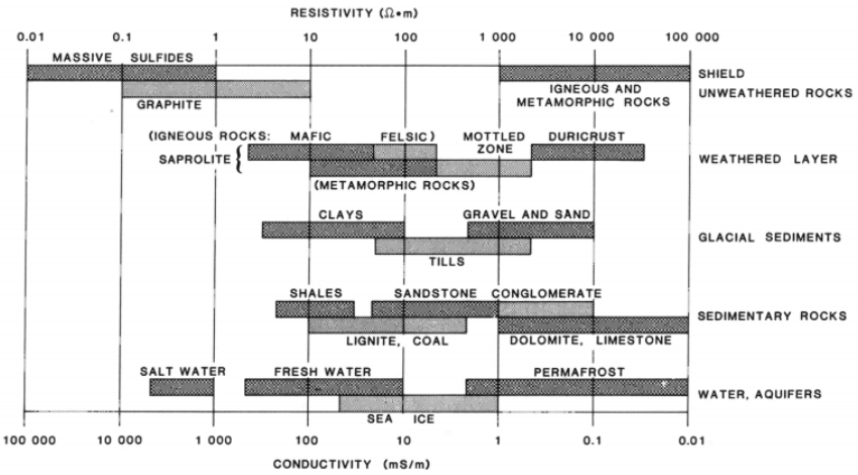

Figure 2.2: Typical conductivity and resistivity ranges for geological targets. (Figure 2 from Palacky (1988)).

For CSEM methods, we reduced Maxwell's equations to Equation 2.17 and Equation 2.18 under the diffusive approximation. In these equations, the only physical properties present are the electrical conductivity and the magnetic permeability. The former changes seven orders of magnitude for standard geological targets and the latter stays the same for most materials except some metals. As a consequence, the electrical conductivity is the most influential material or rock parameter in CSEM methods.

2.3 CSEM noise

In literature (Ziolkowski & Slob, 2019), five different noise sources are discriminated. These are: electrode noise; magnetotelluric noise; cultural noise; motionally induced electromagnetic induction noise; and electronic system noise. The total noise at an electric dipole receiver in voltage is expressed as follows by Ziolkowski and Slob (2019):

$$N_T(t) = V_E(t) + \Delta x_r \left[E_M(t) + E_C(t) + E_I(t)\right] + V_S(t). \tag{2.20}$$

Where:

N_T: Total noise voltage at electric dipole receiver.
V_E: The noise voltage of the two electrodes.
E_M: Magnetotelluric electric field.
E_C: Cultural noise field.
E_I: Motionally induced induction noise.
V_S: Electronic system noise.
Δx_r: Receiver length (distance between the two electrodes).

The noise floor is the sum of all unwanted signals. In the case of an electric dipole receiver, it is N_T, given by Equation 2.20. Below the noise level, signals become much more difficult to detect

as a signal and are easily regarded as noise. To achieve better results, signals can be sampled for a longer time to rise above the noise floor. In analogy with seismic geophysical methods, this is sometimes called stacking. In frequency domain CSEM the noise floor at 1 Hz and 100-s of stacking is around 10^{-15} $\mathrm{V}/(\mathrm{A}\,\mathrm{m}^2)$ and for corresponding time domain CSEM methods it is around 10^{-14} $\mathrm{V}/(\mathrm{A}\,\mathrm{m}^2)$ (Constable, 2010). In the first fully academic marine CSEM and MT survey Myer, Constable, Key, Glinsky, and Liu (2012) found similar values. The noise floors they found, for respectively electric and magnetic field data, were: 10^{-15} $\mathrm{V}/(\mathrm{A}\,\mathrm{m}^2)$ and 10^{-18} $\mathrm{T}/(\mathrm{A}\,\mathrm{m})$. For time domain electromagnetic receivers on the seafloor Li and Constable (2010) state a threshold of around 10^{-15} to 10^{-14} $\mathrm{V}/(\mathrm{A}\,\mathrm{m}^2)$ for a transmitter with an electric dipole moment of $100\ \mathrm{kA}\,\mathrm{m}$.

In our case, the interest lies in the time domain noise floor. The effects we want to observe in our research have to be significantly larger than the noise floor. The research from Myer et al. (2012) gives as well a TDEM noise floor of 10^{-18} $\mathrm{T}/(\mathrm{A}\,\mathrm{m})$. If we multiply this value by the dipole moment of our source and divide by μ_0, we obtain the noise floor for our simulations.

2.4 Marine UXO

An increasing number of constructions is built in the shallow marine environment, such as oil platforms, pipelines and wind farms. The fact that many seas are polluted with UXO endangers and delays these constructions.

Several UXO types are being found in the shallow marine environment. They can be divided into aerial High Explosive (HE) bombs, artillery shells, naval mines, depth charges, and torpedoes. The aerial HE bombs can end up in the shallow marine environment by airstrikes on marine targets or ammunition dumping. In the Second World War it was common for aeroplanes returning to base to jettison their bombs in order to fly quicker. Artillery shells that were used in naval combat or by anti-aircraft guns (both on ships and coastal mounted) can end up in the marine environment. Many shallow marine seas around the world were contaminated with naval mine fields, most notably in World War I and World War II. Although many post-war clearances have been carried out, naval mines are still being found. Depth charges were used in both naval and aerial attacks on submarines. Together with torpedoes they are more rarely found, but they can be present and pose a risk in that case.

When shells impact on the water they normally have a high velocity. In the water this is slowed down rapidly and the shell follows a trajectory ending up horizontally on the seafloor. (Chu, Fan, & Gefken, 2008). After the deposit the shell environment may be altered predominantly by the mechanisms of scour and bedform migration.

Scour is a hydrodynamic process which removes sediment around structures or objects through the vortex formed in front of the object by fluid motion. This occurs mostly in areas with loose sediments, such as sand. The scour can create a scour hole around a UXO piece. When the hole grows so large the UXO piece falls below the seafloor, the hole can fill up with sediment again (Jenkins, Inman, Richardson, Wever, & Wasyl, 2007). Bedform migration is a sedimentary process caused by moving sediments. In this process the bedforms can co-migrate UXO

pieces. Depending on the local height of migrating beds objects can be buried in them. Which trajectory ordnance exactly follows and how it is migrated on the seafloor is out of scope for this research.

Different UXO types found are of various sizes. A common way of quantifying UXO is by stating the ferrous mass, as this is the property that will matter for both magnemetry and EMI surveys. Depending on the site location considered, the UXO types present may vary. A history desk study is normally performed to show which types are present. A recent study on a part of the Dutch North Sea expects UXO to be present with ferrous masses from 10 kg up to 701 kg (Schuddinck & van den Berg, 2017). Objects with less ferrous mass are harder to detect. Depending on the operation that will be carried out, a different detection threshold may be established. A typical detection threshold that is demanded is a 25 or 50 kg ferrous mass of approximately 0.2 m by 0.6 m up to 3 m below the seabed surface. This is what at least should be detected to preserve safety in that operation. A 50 kg ferrous mass would roughly translate to the British WW2 bomb 'G.P. 250-lb. Bomb Mk 1' of which a schematic drawing is given in Figure 2.3. This is one of the UXO types expected to be present in the study site of Schuddinck and van den Berg (2017).

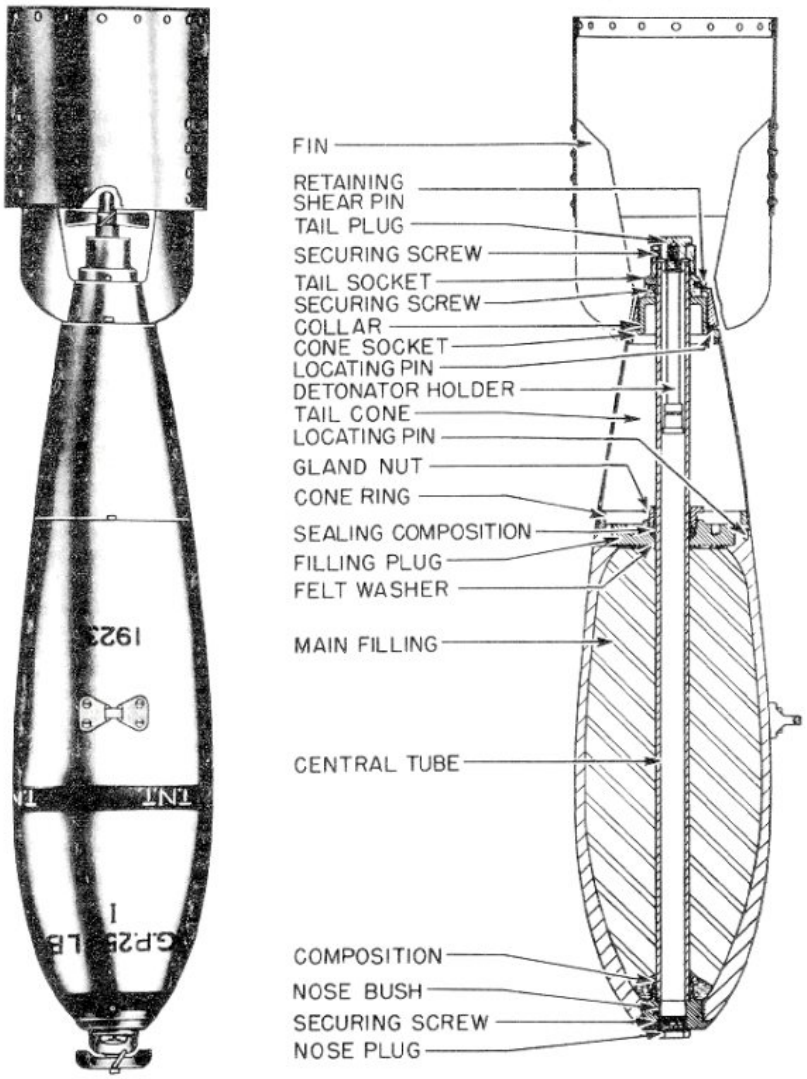

Figure 2.3: British WW2 bomb 'G.P. 250-lb. Bomb Mk 1'. From page 17 of Naval Ordnance Systems Command (1946).

3 | Software validation

The open source Python package SimPEG is a framework for simulation and gradient based parameter estimation in geophysical applications (Cockett et al., 2015). We will be mainly using SimPEG's electromagnetic module (Heagy et al., 2017) to compute electromagnetic responses in the time domain. To verify the results we compute with SimPEG and find out the numerical stability of the simulations done with SimPEG, we compared SimPEG with analytical equations for simple electromagnetic problems. With the help of these reproduction tests we can deduce how to use SimPEG in our further experiments. The properties of the individual meshes created to solve each problem in this section can be found in Appendix B. The generation of two figures with analytical functions and their simulated equivalents is the core result from which this chapter is built around. These figures are given on 18.

The main results of this chapter were also generated using the semi-analytical electromagnetic modelling package empymod by Werthmüller (2017). The results regarding empymod can be found in Appendix C on page 58. The empymod code approximates the analytical functions perfectly with a maximum percent error below 0.04 percent.

3.1 SimPEG simulations

To carry out numerical TDEM simulations with SimPEG the diffusive equations have to be applied in discrete space-time. Therefore, both a spatial and a temporal discretisation have to be made. In this section we describe the process.

Time discretisation

In SimPEG, the temporal discretisation is made by assigning so-called *time steps* to the simulation. These are the steps the SimPEG solver takes in time. The solver uses a first order backward Euler method for the time stepping, which has a first order truncation error. For each new step size the solver has to compute an inverse matrix. The matrix inversion is computationally the most expensive part of the simulation. The most efficient approach to this situation is using the same time step size multiple times, which allows utilising the same inverse matrix multiple times.

In most TDEM problems, one wants to work with a logarithmic time scale, which is hard to sample with just one time step size. Then, the most convenient approach is to use one or two step

sizes per logarithmic decade. This will sample each decade equally and will limit the number of factorised matrices that has to be computed and thus will not cause computational inefficiency.

The scheme we use in the computations in Section 3.2 works as follows: The first point in the time step scheme is right on the lower bound of the time scale we are interested in. Then, for each logarithmic decade in our interest we append 21 times 10^{x-1} and 23 times $3 \times 10^{x-1}$ to our time step scheme, where x stands for the decade. For the last logarithmic decade (i.e. the end of the interval of interest) we do not add time step sizes. For example, if we apply this to the logarithmic interval $[10^{-2}, 10^{0}]$ the resulting array of time steps is, where the subscripts denote the number of the same step size in a row:

$$\begin{aligned}\Big[&10^{-2}, 10_1^{-3}, 10_2^{-3}, ..., 10_{20}^{-3}, 10_{21}^{-3},\\ &3 \times 10_1^{-3}, 3 \times 10_2^{-3} ..., 3 \times 10_{22}^{-3}, 3 \times 10_{23}^{-3},\\ &10_1^{-2}, 10_2^{-2}, ..., 10_{20}^{-2}, 10_{21}^{-2},\\ &3 \times 10_1^{-2}, 3 \times 10_2^{-2} ..., 3 \times 10_{22}^{-2}, 3 \times 10_{23}^{-2}\Big].\end{aligned} \tag{3.1}$$

The distinct points in time, at which the simulation is performed, corresponding to the time step scheme are:

$$\begin{aligned}\Big[&0.000, 0.010, 0.011, 0.012, ..., 0.030, 0.031,\\ &0.034, 0.037, ..., 0.097, 0.100,\\ &0.110, 0.120, ..., 0.300, 0.310,\\ &0.340, 0.370, ..., 0.970, 1.000\Big].\end{aligned} \tag{3.2}$$

The result of applying this scheme to the logarithmic interval $[10^{-2}, 10^{0}]$ is visualised in Figure 3.1. In this figure, the blue line marks the start of the interval (10^{-2}), the red line marks the end of the interval (10^{0}), and the purple points are all the time points in our scheme.

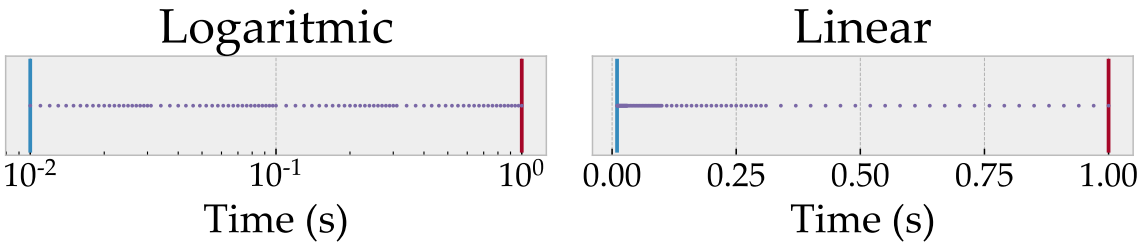

Figure 3.1: A logarithmic time interval sufficiently sampled by time steps. Blue bar: start of interval; Red bar: end of interval; Purple dots: time steps.

Spatial discretisation

In general it is a good idea to create a spatial grid that is larger then the maximum diffusion distance the electromagnetic field will reach in the time span given. In addition to this, the grid cells have to be smaller then the minimal diffusion distance. When these two conditions hold, the problem can be solved without spatial numerical errors. The diffusion distance can be approximated by calculating the skin depth with Equation 3.3 (Adapted from Whittall and Oldenburg (1992)). In this equation δ is the skin depth in metres, t can be any sample time in seconds and σ any model conductivity in $\mathrm{S/m}$. By putting in the minimal time and maximal conductivity value, the minimal distance can be determined and by putting in the maximal time and the minimal conductivity value, the maximal distance can be determined.

$$\delta = 503 * \sqrt{\frac{t}{\sigma}} \tag{3.3}$$

The minimum distance may be of orders smaller than the maximum distance. The simplest mesh one can think of, which uses cells smaller than the minimum distance and extends to more than the maximum distance, is computationally very expensive. Computationally it is more efficient to use a mesh that uses small cells in the area of interest and extends the cell size outwards. The meshes used for the simulations in this section are so-called tensor meshes. They consist of rectangular cells that are fine in the area of interest and expand with coarser cells outwards. These meshes can be characterised by the core cell width, the number of core cells, the number of padding cells, and the expansion factor in the padding cells. The core cell width is the width of cells in the area of interest. The padding cells are the cells outside the 'core'. They become larger outwards as the cell width is multiplied with the expansion factor. In practice, expansion factors higher then 2 should be avoided and according to 'urban legend' the 'magic' number is 1.3 (Haber, 2014). For each of the simulations these values can be found in Appendix B. For horizontal symmetric problems computational cost can be reduced even further by using cylindrical tensor meshes. Cylindrical meshes for horizontal symmetric problems only have discretisation in the negative z, positive z, and positive x direction. The results can then be rotated around the origin to acquire the result in other directions.

3.2 Analytical equations

To validate our computations with SimPEG, we test the package first. We test it by using models and survey setups for which analytical solutions are known. Using SimPEG we want to recreate these analytical solutions and achieve outcomes as close as possible. In this section, we first will explain two different settings for which analytical solutions are known. Then, we show the results and errors for these settings. Finally, we show two possible mistakes that can be made when computing these results.

Vertical magnetic dipole

In the book by Nabighian (1991, p. 215), Ward and Hohmann derive Equation 3.4 and Equation 3.5 for the vertical magnetic field and the time derivative of the vertical magnetic field

respectively, which agrees with the expressions given by Kaufman and Keller (1983). These equations are valid for a homogeneous earth, represented by an infinite half-space, and an infinite half-space of air on top of it. Both the source and receiver are on the interface between air and earth. In these equations m is the magnetic moment of the dipole, x stands for the receiver offset, ρ for the resistivity of the earth. The air resistivity is assumed infinite. The expressions of Ward and Hohmann are given by:

$$h_z = \frac{m}{4\pi x^3}\left[\frac{9}{2\theta^2 x^2}\text{erf}(\theta x) - \text{erf}(\theta x) - \frac{1}{\pi^{1/2}}\left(\frac{9}{\theta x} + 4\theta x\right)\exp(-\theta^2 x^2)\right], \text{ and} \tag{3.4}$$

$$\frac{\partial h_z}{\partial t} = -\frac{m}{2\pi\mu_0\sigma x^5}\left[9\,\text{erf}(\theta x) - \frac{2\theta x}{\pi^{1/2}}(9 + 6\theta^2 x^2 + 4\theta^4 x^4)\exp(-\theta^2 x^2)\right]. \tag{3.5}$$

In these two expressions θ is given by the following equation, in which t is time and μ_0 the permeability of free space.

$$\theta = \sqrt{\frac{\mu_0}{4\rho t}}. \tag{3.6}$$

We used the test example from Ward and Hohmann to recreate the figure given in Nabighian (1991, p. 215). This example is schematically shown in Figure 3.2. A magnetic dipole source and a point receiver are placed on the interface of a half-space earth and a half-space of air. The red star indicates the magnetic dipole source of unit dipole moment, which is shut down abruptly at zero time. The resistivity of the earth is 100 $\Omega\,\text{m}$ and the resistivity of air is assumed at 10^8 $\Omega\,\text{m}$.

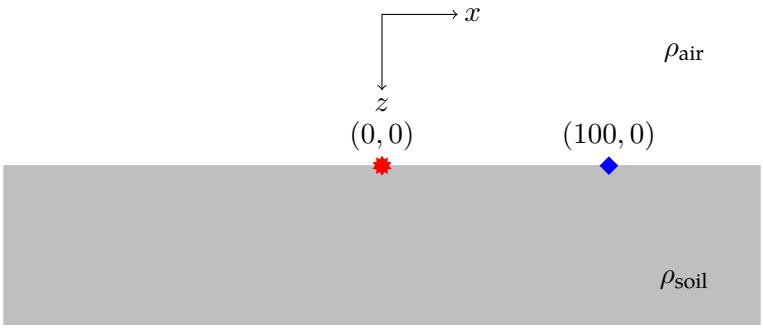

Figure 3.2: Vertical magnetic dipole setup, units in metres. Red star: magnetic dipole source, blue diamond: receiver.

Loop

Also in Nabighian (1991, p. 221), Ward and Hohmann derive Equation 3.7 and Equation 3.8 for the vertical magnetic field and its derivative for a loop source that is abruptly shut down and a receiver in the centre of the loop. In these equations I is the current in the loop before shutdown, a is the loop radius, and θ is given by Equation 3.6. These equations are valid for the same homogeneous earth used in Section 3.2 and are given by:

$$h_z = \frac{I}{2a}\left[\frac{3}{\sqrt{\pi}\theta a}e^{-\theta^2 a^2} + \left(1 - \frac{3}{2\theta^2 a^2}\right)\text{erf}(\theta a)\right], \text{ and} \tag{3.7}$$

$$\frac{\partial h_z}{\partial t} = -\frac{I}{\mu_0 \sigma a^3}\left[3\,\mathrm{erf}(\theta a) - \frac{2}{\pi^{1/2}}\theta a(3 + 2\theta^2 a^2)\exp(-\theta^2 a^2)\right]. \tag{3.8}$$

We used the test example from Ward and Hohmann to recreate the figure given in Nabighian (1991, p. 221). In Figure 3.3 the setup is shown. The $50\ \mathrm{m}$ radius loop source is oriented parallel to the interface of the two half-spaces and is abruptly turned off at zero time. The vertical magnetic field and its derivative are measured right at the centre of this loop. Just as in the dipole setup the resistivity of the earth is $100\ \Omega\,\mathrm{m}$ and the resistivity of air is assumed at $10^8\ \Omega\,\mathrm{m}$.

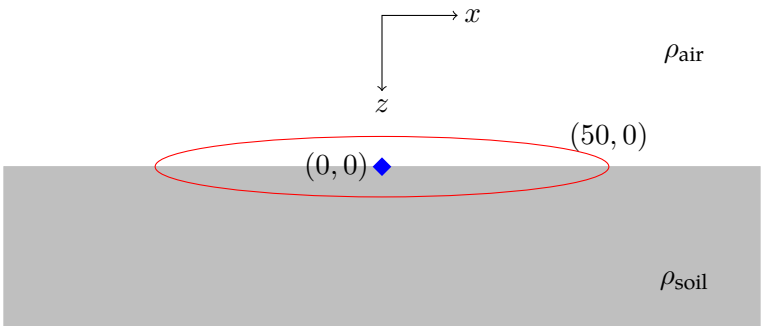

Figure 3.3: Loop source setup, units in metres. Red circle: loop source, blue diamond: receiver.

Results and errors

In Figure 3.4a the test example for a dipole source from Ward and Hohmann is recreated. The top black curve is defined by Equation 3.4 and is the vertical magnetic field and the bottom black curve is defined by Equation 3.5 and is the derivative of the vertical magnetic field. The dotted blue lines are the simulated results using SimPEG. All values are absolute values. The steep dip in all curves near $t = 10^{-2}\ \mathrm{s}$ is where the sign flips. The SimPEG simulations show here the ability to compute a consistent solution that almost fits the analytical solution.

In Figure 3.4b the test example for a loop source from Ward and Hohmann is recreated. The upper black curve is defined by Equation 3.7 and is the vertical magnetic field at the receiver. The lower black curve is defined by Equation 3.8 and is the derivative of the vertical magnetic field at the receiver. The dotted blue lines are the results of the SimPEG simulations. All values are absolute values. Just as the results for the dipole setup explained in Section 3.2 the SimPEG simulations for the vertical magnetic field do not blow up or are off.

Although the computed results may look almost similar to the analytical solutions, there are some differences. To describe those differences, we computed the percent error between the simulated result and the analytical solution. The percent error E_p between a value v and its approximation v' (Rice, 2006) is computed with:

$$E_p = 100 * \frac{|v - v'|}{|v|}. \tag{3.9}$$

In Figure 3.5 the computed percent errors are plotted against the receiver recording time. The following findings can be observed in this figure. For the dipole setting, there is an error of

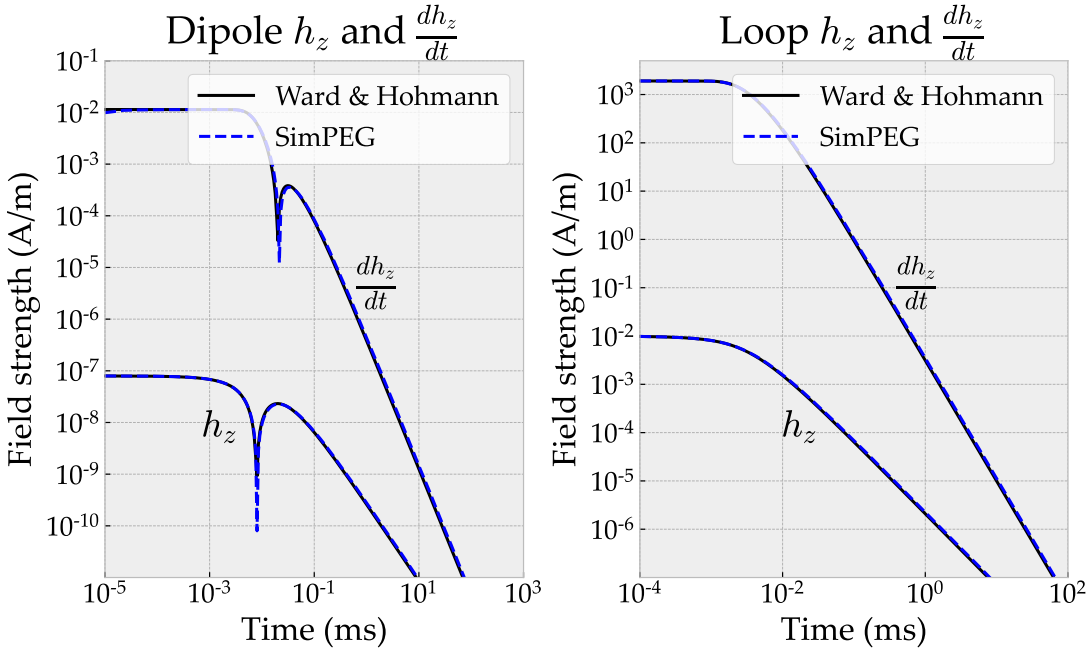

(**a**) Dipole source and point receiver (**b**) Loop source and point receiver

Figure 3.4: SimPEG results compared with analytic solutions. Both are absolute values.

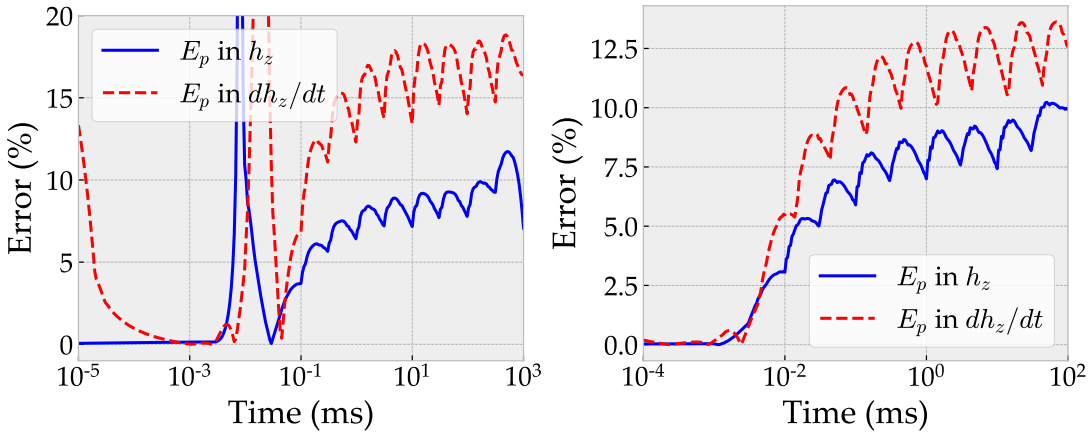

(**a**) Dipole source and point receiver (**b**) Loop source and point receiver

Figure 3.5: Percent errors between SimPEG simulations and analytical solutions.

around 15% in the derivative of the magnetic field at the earliest times. For both the dipole and the loop setting, there is a increasing error, with periodic behaviour, for both the vertical magnetic field and its derivative in the late times ($t > 10^{-1}$ s). These periods have the length of half a logarithmic time decade. The late time error is the largest in the derivative of the vertical magnetic field. Around the sign flip in the dipole setting, the largest errors occur. The percent error in the derivative of the vertical magnetic field even becomes larger than 200 (Not visible in the figure; the maximum value was clipped to 20% to make the other values clearer.). This extreme error is an artefact of the relative error equation. Once a signal goes to zero by the sign flip, the error blows up.

The error in the earliest times in the derivative of the vertical magnetic field is scaling with the smallest cell size. When we computed the same simulations with larger core cells in its mesh, this error became larger, and vice versa for smaller core cells. At time steps this small, the mesh has to be very fine to compute results accurately. The increasing errors in the late times ($t > 10^{-1}$ s) occur due to two different reasons. Generally, at later times an error starts to grow due to the mesh cells that are expanding outwards. For both of the simulations an expansion factor of 1.3 was used. If the expansion factor of the mesh is lower, this error is also lower. On top of that, the time discretisation causes error. The two different time step sizes per logarithmic time decade explain the two periods per logarithmic time decade seen in the error curve.

An explanation for the error growing over time lies in the discretisation scheme the SimPEG framework uses for time stepping. As mentioned before, the time stepping scheme used is first order backward Euler. In a first order method, the error scales with the time step size, which is also visible in the errors we computed.

Possible discretisation errors

In Figure 3.6 two possible errors in the result computed with SimPEG are shown. The cause of the errors lies in the discretisation of the problem. These errors were made in solving the problem described in Section 3.2, where we compute the vertical magnetic field and its derivative from dipole source that is shut down at time zero. These computations are then compared with the analytical solution. For both plots, the top lines are the derivative of the vertical magnetic field, and the bottom curves represent the vertical magnetic field. Both of the errors shown are made in the computation of the vertical magnetic field. The black lines are analytical solutions and the dashed blue lines the SimPEG simulation results. The problem for which these curves are computed is described in Section 3.2. In Figure 3.6a the air resistivity value set to 2×10^{14} $\Omega\,\mathrm{m}$. In analytical formulas this can be assumed infinite to acquire a closed form solution, but when using numerical solvers, extremely large numbers may cause errors. Due to this error, the computed solution is shifted off the analytical solution. In Figure 3.6b we used a mesh that was around four orders too small to account for the diffusion distance of the electromagnetic field. After 10^{-1} ms, the solution starts to blow up. In Figure 3.6a this does not happen, because a sufficiently large mesh was used.

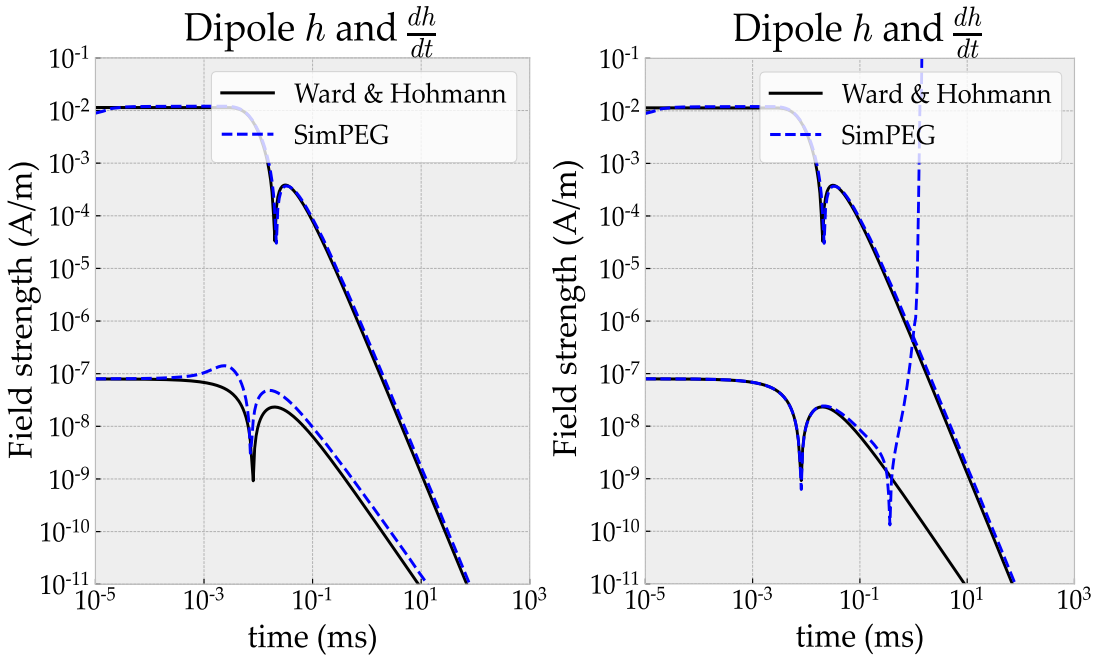

(**a**) Amplitude shift in solution. (**b**) Solution blows up after 10^{-1} ms.

Figure 3.6: Possible simulation artefacts due to (a) too large air resistivity and (b) too small domain size.

3.3 Extension to fields

Receiver array

In Equation 3.4 and Equation 3.5 the receiver offset from the source is the parameter x. When we change this parameter to different values we can calculate the response at different offsets. This way we can simulate the responses a line of receivers would receive from a dipole source and can also check the results with the analytic formula. In the SimPEG simulation this will not cause more computational cost, because it can handle multiple receivers in one simulation.

We chose to simulate a two kilometre line of 100 equally spaced receivers, with the dipole source at the origin. The receivers measure the derivative of the vertical magnetic field from $t = 10^{-8}$ s to $t = 10^{0}$ s. This is the same time span used in Section 3.2. In Figure 3.7 the result of the SimPEG simulation is shown, together with the analytical solution and the percentage error of the simulation with respect to the analytical solution. The characteristics of this mesh are in Appendix B. The time discretisation scheme used is the same as the scheme described in Section 3.1.

The resulting error in Figure 3.7 may look complicated, but the same error artefacts as in Section 3.2 can be observed. Between $t = 10^{-8}$ s and $t = 10^{-7}$ s the error is over 20%, caused by the combination of really small time steps and spatial cells being too large. At the sign change in the field there is again a large error, noticeable by the curved yellow line. Hereafter, the periodically

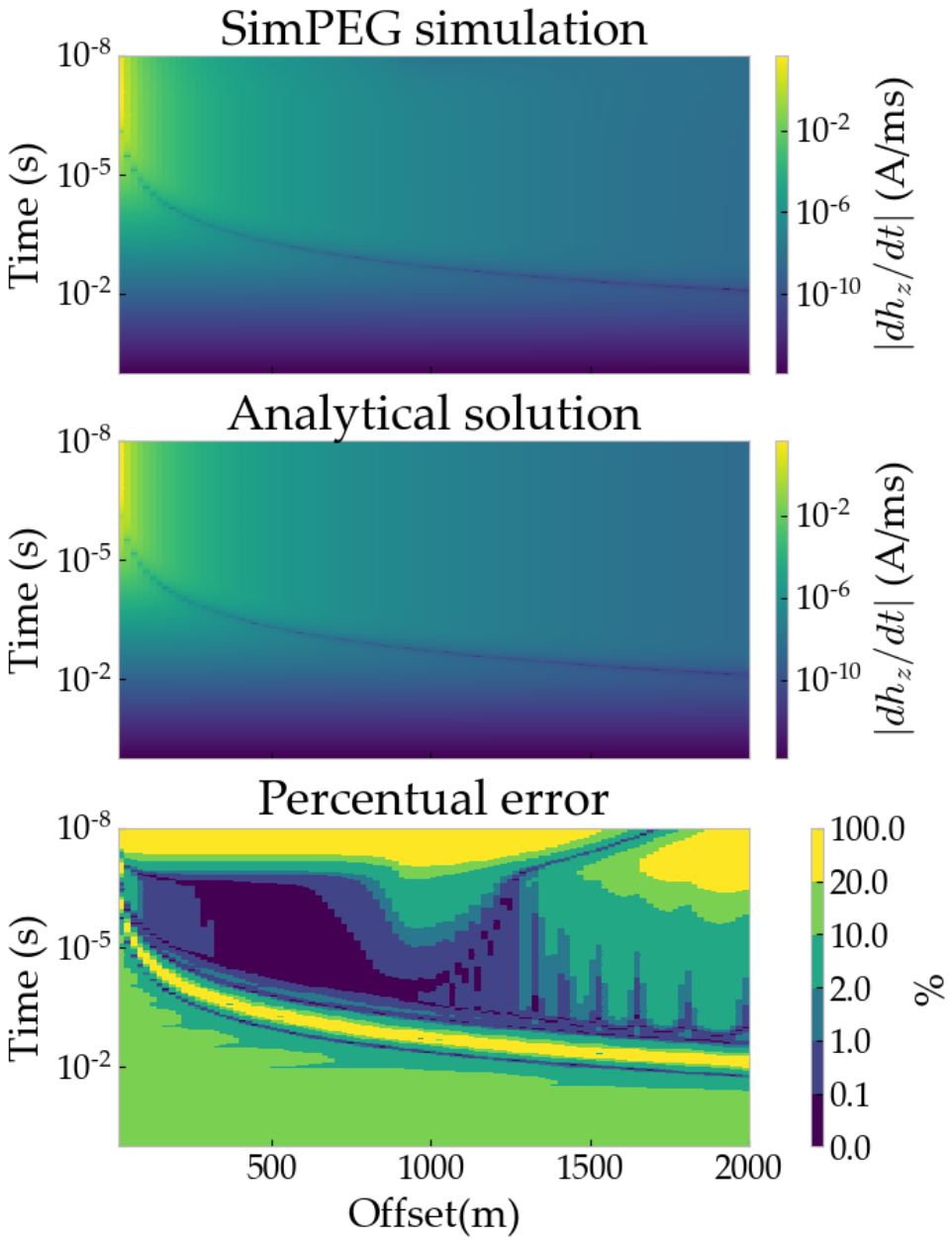

Figure 3.7: Dipole impulse response for a line of receivers. Top: simulated response; Middle: analytical response; Bottom: percentage error.

repeating behaviour in the error can be observed again. Next to these earlier observed error behaviours there are some new artefacts. Roughly between offsets $x = 1000$ m and $x = 2000$ m, the error starts to rise. This is caused by the expanding cells of the mesh. Until $x = 900$ m core cells of size 3 m are used. For all greater offsets the cell size is expanding with the expansion factor of the mesh, which was set to 1.2.

Field progression

Just as we extended the dipole setup, we can extend the loop setup. For the same homogeneous half-space earth as before we use the same 50 metre loop. We use two metre spaced receivers from the centre of the loop radially outwards. They record between 10^{-6} and 10^{-3} seconds from loop shutoff. In Figure 3.8 a snapshot of the vertical magnetic field at each logarithmic decade is shown. The radial axis is defined in metres and points outward from the centre.

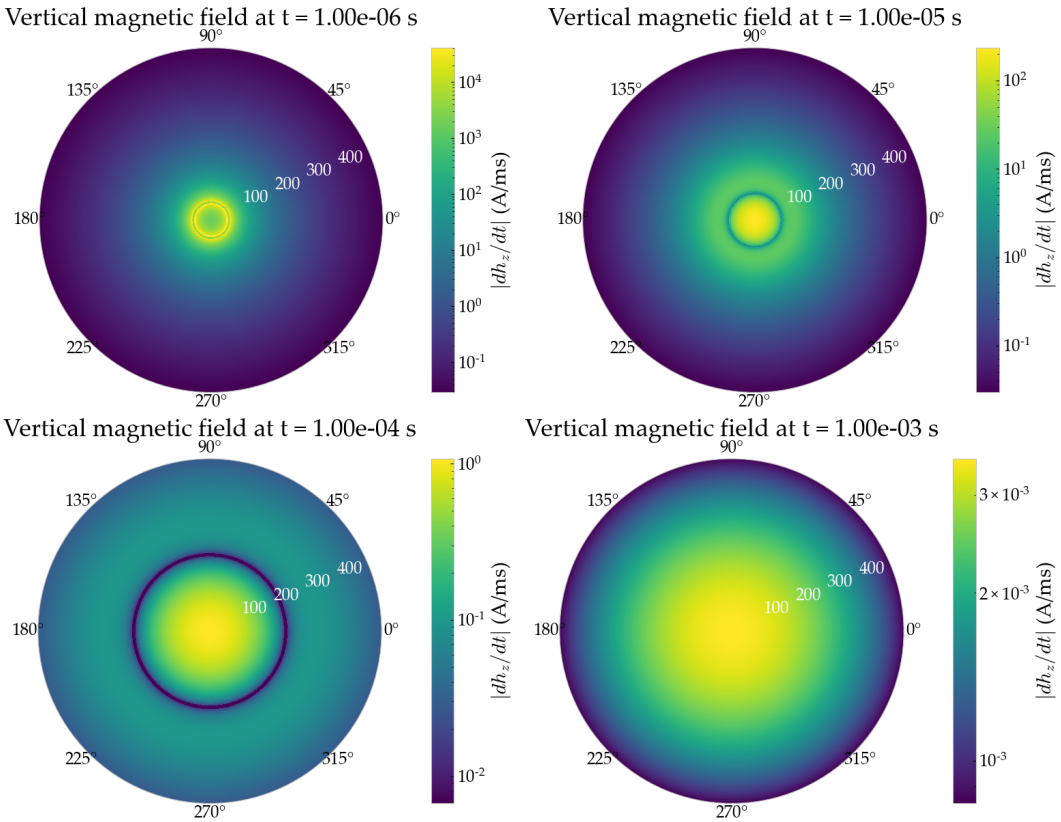

Figure 3.8: Vertical magnetic field progression after loop shutoff at four different logarithmic spaced times.

3.4 Conclusions for simulations with SimPEG

In this chapter we conducted multiple experiments with SimPEG. We compared simulated results to analytical equations, first for a dipole source with one receiver and second for a loop source with one receiver. Then, we extended these simulations to multiple receivers to compute fields over time. Again, we did this first for the dipole source and second for the loop source. In the cases of a dipole source and one receiver, a loop source and one receiver, and a dipole source and multiple receivers, we compared the results with analytical equations. For all three cases a percent error was computed. Respectively for the three cases the errors are plotted in Figure 3.5a, Figure 3.5b, and Figure 3.7.

From the simulations computed and the comparison to analytical solutions, we can draw a number of conclusions for further simulations:

1. The time window of interest for a certain simulation should be sampled everywhere in this window, but should ideally not use too many different time step sizes for the sake of computational time. For example, two different time step sizes per logarithmic decade in the time window of interest work well.
2. The model should be carefully discretised into a spatial mesh. The mesh should be small enough around areas of interest, such as the source or parameter boundaries. It is small enough when it's smaller then the minimum diffusion distance around the source and when boundaries are on their physical location. Not taking care of this causes errors in the earliest time steps. On top of this, the mesh should extend far enough to account for the maximum diffusion distance.
3. To create a large mesh, the mesh cells can be made larger outwards from the centre of the mesh with the expansion factor. Higher expansion factors cause more error at later times in the simulation. Keeping the expansion factor low helps to suppress this error. Expansion factors above 2 should be avoided. Thus, accepted values for the expansion factor are between 1 and 2.
4. Extreme conductivity or resistivity values ($10^{10}\,\Omega\,\mathrm{m}$ or more, $10^{-10}\,\mathrm{S/m}$ or less) may cause extreme errors. They are hard to handle for the solver and can cause a blow up in the solution. It is best to not use such extreme values.
5. In our simulations we find an error increasing over time. In the derivative of the magnetic field this error is the largest. For the dipole source this error is 19 percent or lower, for the loop source 14 percent or lower. The source of this error is the first order backward Euler scheme SimPEG uses for the time stepping. By implementing a second order method this error could most likely significantly be decreased, however at the cost of computation speed.

To get the best out of both worlds and achieve consistent results with reasonable computational cost the first thing we will do in our further simulations is use a coarse time sampling scheme and a mesh with a minimal number of cells, in order to just produce consistent results. Then, when consistency is found on a certain simulation, it should be computed with a finer time sampling scheme and a finer mesh to decrease the errors as far as possible.

4 | Sensitivity analysis

Now that we established the limits of the software, we use it to answer the research questions we posed in Chapter 1. In this chapter we investigate the influence of the target's parameters on the response signal with the goal to find out how these parameters are related to the recorded signal. First we introduce the marine model along with an overview of the parameters we evaluate in this model. Then, we discuss the survey setup used in the model. After that, we define the measurability and how to quantify the modelled responses. Furthermore, we perform the parameter sensitivity analysis in two different ways. First taking a one-at-a-time approach to find out the individual relations between parameters and modelled response. Second, we take a statistical approach by comparing influences of probable parameters values on the modelled responses between the different parameters. Finally, we explain our characterisation experiment and give an overview of all experiments conducted.

4.1 Marine model

In Figure 4.1 a schematic overview of the marine model is given. It is defined in a three-dimensional Cartesian coordinate system with the positive z axis pointing downwards. The positive y axis is pointing out of the page. The model consists of three layers, from top to bottom: air (white), sea (dark grey), soil (light grey). Each layer has its own conductivity value, respectively σ_{air}, σ_{sea}, and σ_{soil}. The sea layer is the only layer with a finite thickness, which is equal to the depth to the seafloor d_{seafloor}. The air and soil layers are both half spaces. The origin of the coordinate system is defined at the interface between air and sea. Right below the origin, the source is located in the sea layer at depth d_{src}. Consequently, the depth to the source must always be lower than the depth to the seafloor ($d_{\text{src}} < d_{\text{seafloor}}$).

In the model's soil layer, there is an extra feature present. This is the target we are interested in. Regardless of the shape of the target, its depth (d_{target}) is defined from the seafloor to the top surface of the target. This means that for a unit cube target with $d_{\text{target}} = -0.5$ half of the cube is submerged into the soil and the other half is exposed in the sea. We define the target in the model as a hollow cuboid. The parameters length L, width W, and height H define the size and the outer shape of the cuboid in, respectively, the x, y, and z directions. The cuboidal target model has a wall thickness Δx_{wall}. It has two conductivity values, one for the wall (ρ_{wall}) and one for the interior (σ_{interior}). A graph of the cuboidal model is given in Figure 4.2 with annotations of its shape and size parameters.

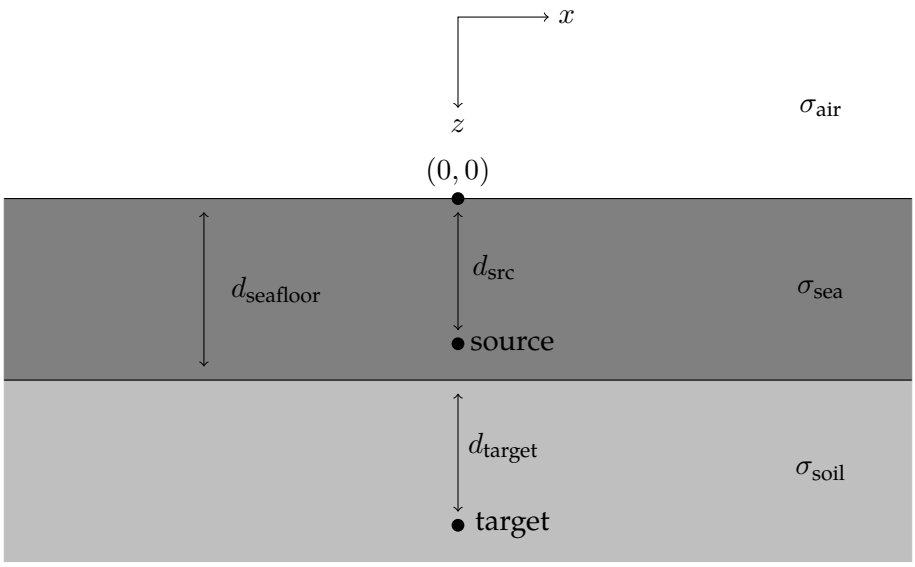

Figure 4.1: The marine model. σ_{air}, σ_{sea} and σ_{soil} are the air, sea and the soils conductivity, respectively.

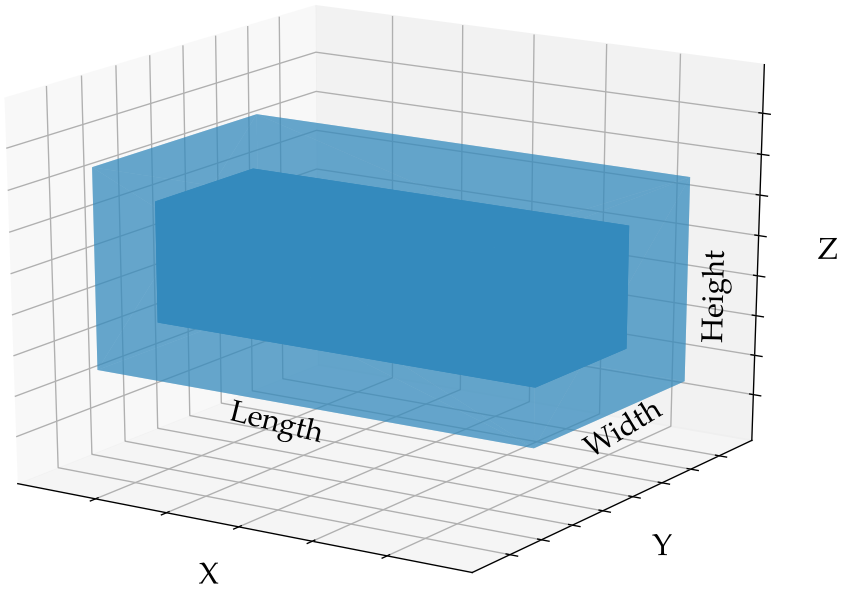

Figure 4.2: Example cuboidal target model. The solid blue colour denotes the target's interior and the transparent blue colour the target's wall.

Actual UXO targets are usually of cylindrical or spherical shape. The target we are modelling is cuboidally shaped. We chose this because we cannot discretise a cylindrical or spherical shape without significant aliasing on a rectangular mesh. Modelling a cylinder properly on a rectangular mesh would require a very fine cell size around the cylinder. This would cause a significant increase in the number of cells and therefore also in the computational cost. Adaptive tetrahedral grid methods can overcome this problem, but they are not implemented in SimPEG. Before this choice was made, we conducted an experiment to test the impact of rotations of the target. This experiment used yaw, pitch and roll rotations around the target's main axis and is described in Appendix D. Our main conclusion of this experiment is that yaw rotations of the target give no significant change to its response, and thus we can keep the target perfectly aligned with the grid.

In this section we introduced many parameters without a given value in our model. An overview of these parameters can be found in Table 4.1.

Table 4.1: Parameters introduced by the marine model.

Symbol	Description	Unit
σ_{air}	Air conductivity	$\mathrm{S/m}$
σ_{sea}	Sea conductivity	$\mathrm{S/m}$
σ_{soil}	Soil conductivity	$\mathrm{S/m}$
σ_{wall}	Target wall conductivity	$\mathrm{S/m}$
σ_{interior}	Target interior conductivity	$\mathrm{S/m}$
d_{src}	Depth from sea level to source	m
d_{seafloor}	Depth from sea level to seafloor	m
d_{target}	Depth from seafloor to target	m
L	Length of target (x directed)	m
W	Width of target (y directed)	m
H	Height of target (z directed)	m
Δx_{wall}	Wall thickness	m

4.2 Survey setup

In TEM methods a primary electromagnetic field is induced into the ground by the antenna. Most commonly, this antenna is a wire coil. The source strength is given by the magnetic dipole moment τ. This is the product of the number of turns N, the current I, and the area of the coil A. This relationship is given by:

$$\tau = NIA. \tag{4.1}$$

The receiver antenna is most commonly also a coil. The rate of change in the secondary field, produced by eddy currents in the ground after shutoff of the transmitter, is measured with the proportional flux through the receiver coil. In practice, a lot of different coil sizes are used. Devices vary from a single coil source and receiver ("EM61MK2 Operating Instructions", 2011)

to arrays of receivers and transmitters (Prouty et al., 2011). As the actual design of a TEM device is out of our scope, we define the simplest setup that enables us to answer the research questions. We use a circular loop antenna, with a radius of $0.5\ \mathrm{m}$, a current of $1\ \mathrm{A}$, and only one winding as source. This corresponds to a dipole moment of $0.25\pi\ \mathrm{A\,m}$. The receiver antenna is modelled as a point in the middle of the loop and can measure the derivative of the magnetic field in x, y, and z directions.

4.3 Signal analysis

In a hypothetical setup we can distinguish between two different signal functions. The target signal function $f_{\text{target}}(t)$, acquired on a model with a target, and the background signal function $f_{\text{background}}(t)$, acquired on the same model without target. To compare different setups we need to assess how visible their target signals are over the background signal. This can be done in a consistent manner by computing the area of the absolute difference between the two functions on a certain time span $[t_0, t_1]$. We call the area between the curves the **net effect**, denoted with $\mathcal{N}$. From the net effect, and information about the noise, the measurability can be determined. The measurability will say if a certain signal is measurable. So to assess our measured signal, we have two different values, in ascending order of strictness:

1. Net effect
2. Measurability

In this section we first explain the net effect, followed by the measurability.

4.3.1 Net effect

For a general setting with two functions f_1 and f_2 the area on a certain time span $[t_0, t_1]$ is visualised in Figure 4.3. The net effect area for this setting can be calculated with the following equation:

$$\mathcal{N} = \int_{t_0}^{t_1} |f_1(t) - f_2(t)|\,\mathrm{d}t. \tag{4.2}$$

The functions may be given on a logarithmic scale. This causes the function points to be spaced irregularly. For irregularly spaced data the integral can be approximated numerically with the composite Simpson's rule by dividing the interval $[t_0, t_1]$ into an even number N sub-intervals of widths h_k. This is expressed as follows (Vuik, Vermolen, Gijzen, & Vuik, 2007):

$$\int_{t_0}^{t_1} f(t)\mathrm{d}t = \sum_{i=0}^{N/2-1} \left(\alpha_i f_{2i+2} + \beta_i f_{2i+1} + \eta_i f_{2i}\right), \tag{4.3}$$

where $f_k = f\left(t_0 + \sum_{i=0}^{k-1} h_i\right)$ are the function values at the k^{th} point on the interval $[t_0, t_1]$, and

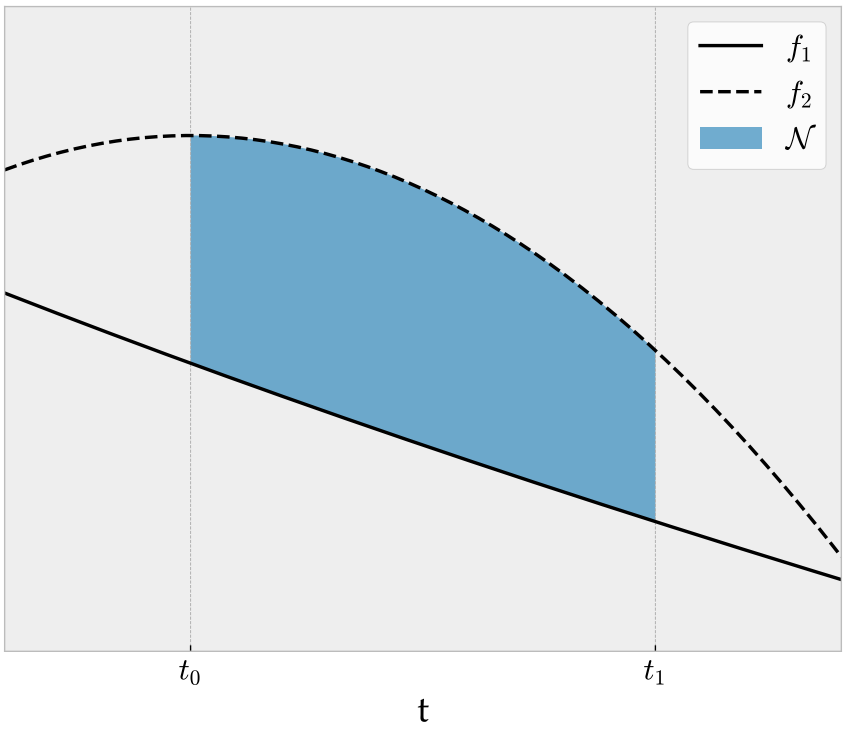

Figure 4.3: Area between two curves on a given time interval (the net effect).

the coefficients α_i, β_i, and γ_i are given by:

$$\alpha_i = \frac{2h_{2i+1}^3 - h_{2i}^3 + 3h_{2i}h_{2i+1}^2}{6h_{2i+1}\left(h_{2i+1} + h_{2i}\right)}, \tag{4.4}$$

$$\beta_i = \frac{h_{2i+1}^3 + h_{2i}^3 + 3h_{2i+1}h_{2i}\left(h_{2i+1} + h_{2i}\right)}{6h_{2i+1}h_{2i}}, \text{ and} \tag{4.5}$$

$$\eta_i = \frac{2h_{2i}^3 - h_{2i+1}^3 - 3h_{2i+1}h_{2i}^2}{6h_{2i}\left(h_{2j+1} + h_{2i}\right)}. \tag{4.6}$$

For an even number N of sub-intervals the last or first step needs to be approximated differently, for example with the trapezoidal rule. For an odd number of samples and thus an even number of sub-intervals, that are equally spaced, the result is exact if the function is a polynomial of third order or less. For irregularly spaced samples, the result is exact if the function is a polynomial of second order or less. By making the substitution $f(t) = f_1(t) - f_2(t)$ in Equation 4.2 and applying the composite Simpson's rule we end up with the following equation:

$$\mathcal{N} = \left| \sum_{i=0}^{N/2-1} \left(\alpha_i f_{2i+2} + \beta_i f_{2i+1} + \eta_i f_{2i}\right) \right|. \tag{4.7}$$

With the obtained equation we can quantify the net effect of a certain signal in a consistent manner. On a linear as well on a logarithmic time scheme.

4.3.2 Measurability

On every TEM measurement there are limiting factors. We distinguish between the following ones:

- Time resolution
- Noise level
- Signal noise (including water effects)

The time resolution defines the smallest time interval that possibly could be recorded. If a signal produces net effect before this smallest time interval, it is not measurable. The noise level, introduced in Section 2.3, defines the smallest amplitude that could be recorded. Signals with amplitudes below the noise level are hard to distinguish from the noise. Stacking and signal processing can be used to distinguish those signals. The signal noise includes all noise that is perceived as normal signal. This includes the effects of the moving water. Signal noise is an uncertainty percentage around the true signal. In practice, this percentage can be determined by carrying out the same measurement a couple of times and investigating the variation in the responses.

These three effects can be incorporated in our net effect computation to acquire a single value measurability of a signal. The limiting factors act as constraints to the computed area and the remaining area is the **measurable net effect**, which we call the **measurability** and denote with $\mathcal{M}$. The constraints are shown in Figure 4.4, by limiting the net effect from Figure 4.3 into measurability. The minimal time and the noise level appear as linear constraints. Signal noise is visible as a continuous error percentage for both f_1 and f_2.

In our experiments we use the conditions given in Table 4.2 for these three constraints. The smallest time resolution is set to 4 microseconds. Modern systems such as the Towed Transient Electromagnetic (tTEM) can record unbiased at such small times (Auken et al., 2019). The noise level is derived from the literature values given in Section 2.3. Multiplying the level given there by the dipole moment of our loop source, and dividing by μ_0 to go from the **b** field to the **h** field yields the noise level we use. In a recent underwater TDEM study the signal noise was on average 3% and was less than 20% for all experiments (Saville, Bancroft, Bell, Odlum, & Steinhurst, 2018). We assume the signal noise on any signal to be 10%.

Table 4.2: Constraints applied to go from net effect to measurability.

Constraint	Mathematical representation	Reference
Time resolution	$t > 4$ µs	Auken et al., 2019
Noise level	$\lvert dh/dt \rvert > 0.625$ pA/m	Constable, 2010
Signal noise	$f \pm 10\%$	Saville et al., 2018

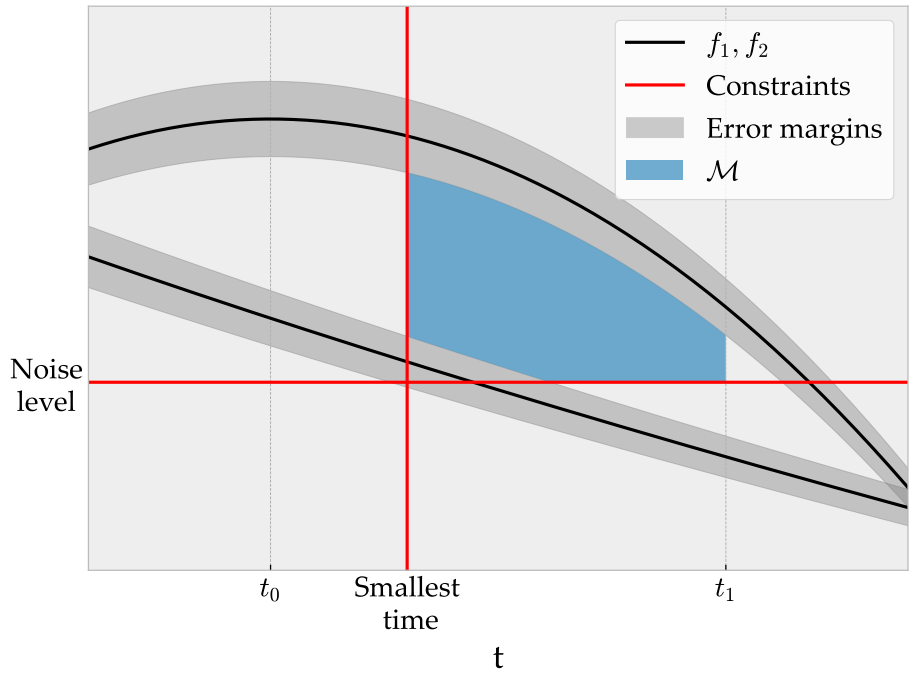

Figure 4.4: Measurable area between two curves on a given time interval (the measurability).

4.4 Sensitivity of model parameters

For every ordnance piece in the marine environment, we can identify some key parameters. Those are: the burial depth, the size, the wall thickness, and the wall's electrical conductivity. Out of the parameters in Table 4.1 these are the ones that vary for every other UXO piece. In our research one of the goals is to determine how these parameters influence the measurability of a signal. Therefore we conduct two sensitivity studies on these parameters. We carry out the first sensitivity analysis using a one-at-a-time approach. We choose standard values, vary a parameter while keeping the rest fixed, and derive the relationship of that parameter with the measurability. This approach is further explained in Section 4.4.1. For the second sensitivity analysis, we take a more statistical approach. We model each parameter with a distribution, and carry out forward simulations with certain points from this distribution. These simulations yield measurability values, which we use to compare the sensitivity of the parameters with each other. This approach is further explained in Section 4.4.2.

4.4.1 One-at-a-time

In the one-at-a-time sensitivity analysis we analyse every single parameter at a time. After we established the default parameter values and the parameters to analyse, our workflow for each parameter is as follows:

1. Compute the TEM response for the marine model without target: the background response.

2. Compute TEM responses for each value the parameter can take.
3. For each simulation, compute the measurability.
4. Analyse the relationship between the measurability and the parameter values.

Our marine model, defined in Section 4.1 comes with wide set of parameters (Table 4.1). For our research, which is focused on the target side of the model, we individually investigate parameters which define the target's geometry. These are the depth of the target below the seafloor, the size of the target, and the wall thickness. We take standard values for every parameter in our model, which are given in Table 4.3 and vary one parameter at a time in the following experiments:

- **Depth:** we investigate targets from lying on the seafloor, to half submerged targets, to buried targets up to five metres depth.
- **Size:** the size is defined by three parameters in our marine model, the length, width, and height of the target. To find out the general relation between the size and the response we define a characteristic size S_c which the three parameters depend on. We vary the characteristic size from 0.4 to 0.15 metres. The width and height equal the characteristic size, and the length equals four times the characteristic size.

  To find out if the horizontal area or the volume of a target is the main influence to the response we additionally carry out the following two size experiments, starting with exactly the same target with initial dimensions $L = 0.1$ m, $W = 0.1$ m, and $H = 0.16$ m:

  - Increasing the horizontal area while the volume stays constant by increasing the length while decreasing the height.
  - Increasing the volume while the horizontal area stays constant by increasing the height, while the length and width stay constant.
- **Wall thickness:** we investigate wall thicknesses from 0.01 to 0.05 metres.

For every parameter value in the experiments, we compute the response. Then, we compare each signal with the background signal, and from that we calculate the measurability. With the measurability we are able to analyse each parameter and determine its relationship with the measurability. We quantify the relationship by fitting a polynomial, which is computed iterative by minimising the error between the fitted points $p(x_j)$ and the given points y_j:

$$min \quad E = \sum_{j=0}^{k} |p(x_j) - y_j|^2 . \tag{4.8}$$

To quantify our final fit one might use the Root Mean Square Error (RMSE), with the fitted values being denoted by $\hat{y}_i = p(x_j)$:

$$RMSE = \sqrt{\frac{\sum_i^N (\hat{y}_i - y_i)^2}{N}}. \tag{4.9}$$

Table 4.3: Marine model parameters with default values for one-at-a-time simulations.

Symbol	Description	Value	Unit
σ_{air}	Air conductivity	10^{-8}	S/m
σ_{sea}	Sea conductivity	3	S/m
σ_{soil}	Soil conductivity	1	S/m
σ_{wall}	Target wall conductivity	10^{7}	S/m
σ_{interior}	Target interior conductivity	10^{-3}	S/m
d_{src}	Depth from sea level to source	49	m
d_{seafloor}	Depth from sea level to seafloor	50	m
d_{target}	Depth from seafloor to target	2	m
L	Length of target (x directed)	0.4	m
W	Width of target (y directed)	0.1	m
H	Height of target (z directed)	0.1	m
Δx_{wall}	Wall thickness	0.01	m

For measurabilities that are changing orders of magnitude, the RMSE can become too sensitive to the extreme values. In this case it is better to use a normalised version. To make it more useful, we use the Normalised Root Mean Square Error (NRMSE):

$$NRMSE = \sqrt{\frac{\sum_i^N (\hat{y}_i - y_i)^2}{\sum_i^N (y_i)^2}}. \tag{4.10}$$

4.4.2 Statistical approach

In our statistical approach we want to compare the sensitivities of different parameters with each other. Just as in the one-at-a-time approach, we use the parameters on the target side of the model. We use the burial depth, the size, wall thickness, and wall conductivity. The size will be determined by the characteristic size S_c. This is defined identically to the one-at-a-time-approach ($S_c = W = H$, $4S_c = L$). All other parameters are set to the default values, see Table 4.3. Our workflow in this approach is as follows:

1. Use a Probability Density Function (PDF) for each of the parameters. When carried out in practice, this step ideally should be done by conducting a site investigation. The site investigation will lead to distributions of the parameter that can be used for the rest of the steps in our statistical approach.

2. Compute the 10th, the 50th, and the 90th percentile of this PDF using the quantile function to get P10, P50, and P90.

3. Set all parameters to P50 and compute the TEM response for this setting. This setting is called the base case.

4. For each parameter carry out another two simulations. One using the P10 value, and the

other using the P90 value. All other parameters are kept to the P50 for both simulations. These simulations are the low and high outcomes for each parameter.

5. Compare the low and high values by plotting them in a tornado chart.

Probability distribution functions

The PDF from probability theory helps us to classify the values these parameters can take. The value of this function at a certain point in the sample space of a parameter can be interpreted as the relative likelihood that the parameter equals this point in sample space. To create an appropriate distribution for each parameter we used different PDFs. The different ones are given with their formula, relevant parameters, and a short explanation below.

In this section all distributions are noted as a function $p(x; ...)$, where x can be any value of the variable distributed. The other defining parameters of the distribution are given after the semi-colon in the function definition. The symbols used for the other defining parameters may conflict with other symbols used in this thesis or even in other distributions given in this section. To avoid confusion, the defining parameters are explained before each distribution is given.

The most commonly used distribution is the normal distribution. This bell shaped peak, defined by the mean μ and standard deviation σ is given by:

$$p(x; \sigma, \mu) = \frac{1}{\sigma\sqrt{2\pi}} \exp\left[-\frac{1}{2}\left(\frac{x-\mu}{\sigma}\right)^2\right]. \tag{4.11}$$

For a parameter that varies many orders of magnitude, the log-normal distribution can make more sense. This distribution will on a logarithmic scale look like a normal distribution on a linear scale. The distribution is defined by the median m and standard deviation σ and is given by:

$$p(x; \sigma, m) = \frac{1}{x\sigma\sqrt{2\pi}} \exp\left[-\frac{(\log(x/m))^2}{2\sigma^2}\right]. \tag{4.12}$$

The normal distribution is continuous for all real values of x. If we have prior knowledge about the variable and know that it only has non-negative real values, a Rayleigh distribution works better. The Rayleigh distribution is only continuous for positive real values. It is defined by the scale factor σ and is given by:

$$p(x; \sigma) = \frac{x}{\sigma^2} \exp\left[-x^2/\left(2\sigma^2\right)\right], \quad x \geq 0. \tag{4.13}$$

Another distribution that is only continuous for positive real values is the chi-square distribution. It is defined by the degree of freedom k and the function is given by:

$$p(x; k) = \begin{cases} \dfrac{x^{\frac{k}{2}-1}\mathrm{e}^{-\frac{x}{2}}}{2^{\frac{k}{2}}\Gamma\left(\frac{k}{2}\right)}, & x > 0 \\ 0, & \text{otherwise,} \end{cases} \tag{4.14}$$

in which the Gamma function is defined as: $\Gamma(n) = (n-1)!$.

Pairing functions with model parameters

In Table 4.4 the distributions we used for the model parameters are given, along with the relevant parameter settings of that particular distribution function. A plot of the probability distribution for the model parameters is given in Appendix E.

Table 4.4: Distribution functions for the investigated model parameters.

Parameter	Symbol	Distribution	Equation	Function parameters
Wall conductivity	σ_{wall}	Log-normal	Equation 4.12	$m = 10^7, \sigma = 1.7$
Characteristic size	S_c	Rayleigh	Equation 4.13	$\sigma = 0.11$
Wall thickness	Δx_{wall}	Rayleigh	Equation 4.13	$\sigma = 0.019$
Target's depth	d_{target}	Chi-squared	Equation 4.14	$k = 2$

Distributions to points

For each variable we can convert the PDF to a Cumulative Distribution Function (CDF) by integrating it. From the CDF we compute its inverse, the quantile function (also called percent-point function). We use the quantile function to determine the P10, P50, and P90. Visually the P10, P50, and P90 can already be determined from the CDF by picking the parameter value corresponding to a CDF of 10%, 50%, and 90%. See the example in Figure 4.5 where the P50 is determined from a CDF corresponding to a normal distribution (Equation 4.11) as PDF. Applying this to the functions defined in Table 4.4 yields the P10, P50, and P90 values in Table 4.5.

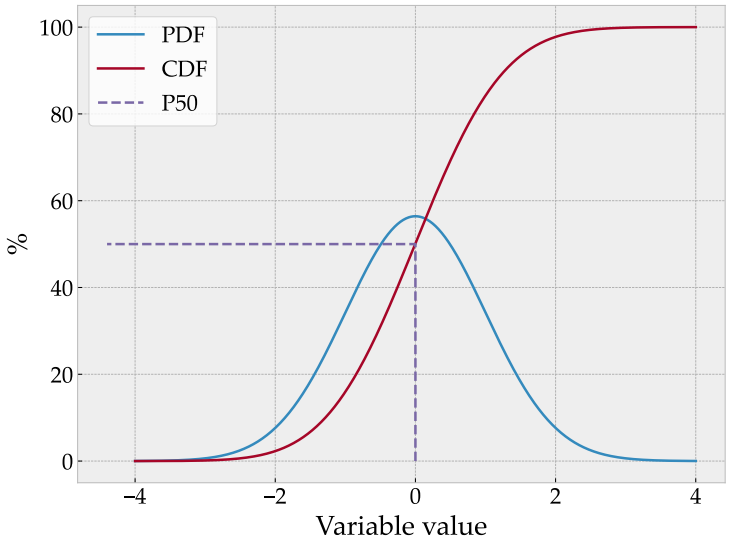

Figure 4.5: Example of determining the P50 from a CDF.

Table 4.5: P10, P50, and P90 values for the investigated model parameters.

Parameter	Symbol	P10	P50	P90	Unit
Wall conductivity	σ_{wall}	62373	549540	4841723	$\mathrm{S/m}$
Characteristic size	S_{c}	0.05*	0.13*	0 24*	m
Wall thickness	Δx_{wall}	0.01*	0.02*	0.03*	m
Target's depth	d_{target}	0.2*	1.4*	4.5*	m

† These values are rounded

4.5 Characterisation experiment

Once a measurable signal is measured, it still has to be determined what actually is measured. This is where a classifier comes in play. The classifier determines whether the signal corresponds to a target of interest, such as UXO, or a target not of interest, for example some scrap, and handles the characterisation of the signal. The actual classifier is out of scope of our research, but to find out what the influence of a metal piece not of interest on the response is, we conduct a characterisation experiment. In our marine model, we add an additional object. This object is modelled as a metal plate with dimensions $L = 0.1$ m, $W = 0.1$ m, and $H = 0.01$ m. It is placed directly on the seafloor.

4.6 Overview of experiments

To summarise, here we give an overview of all experiments conducted.

- One-at-a-time approach
  - Burial depth
  - Target size
    - Characteristic size
    - Area versus volume
  - Wall thickness
- Statistical approach for relative significance
- Characterisation experiment

5 | Results and discussion

In this chapter we show and discuss the results of our sensitivity analysis on TEM responses of marine UXO. The methodology of this analysis is explained in Chapter 4. In this methodology, two approaches have been discussed. The one-at-a-time approach, focused on the impact of individual parameters to the UXO response, and the statistical approach, focused on the relative significance of the impact of different parameters on the UXO response. We first give the results of the one-at-a-time approach in Section 5.1 and the results of the statistical approach follow in Section 5.2. Then, we show the results of our characterisation experiment in Section 5.3. Finally, we discuss the results in Section 5.4.

5.1 Individual parameters

In our marine model, the parameters defining the target are its depth below the seafloor, its size, and the wall thickness. In Section 4.4.1 we defined simulation experiments that can be quantified with the net effect and measurability. The net effect and measurability were defined in Section 4.3. For the depth and wall thickness we conducted a single experiment, for the size we used two approaches. In this section we discuss the results of all conducted experiments on single parameter influence. For the first parameter to be discussed, the depth, we show all relevant figures here. For the other parameter experiments, we only show the final figures here. Additional result figures can be found in Appendix C.

5.1.1 Depth

The computed signals in our one-at-a-time depth experiment are plotted in Figure 5.1 together with the background response. The darker red a signal is in this plot, the closer to the seafloor the target is. Consequently, the signals closer to the seafloor have larger amplitudes and are visible for a longer time. This is made more clear in Figure 5.2, where the computed signals are divided by the background response to yield the signal to background ratio for each signal. Again, the more red curves are closer to the seafloor. Here it is visible that targets closer to the seafloor produce more signal which is visible at earlier times.

For every computed signal, we computed the net effect and measurability. The computed values for each depth are plotted against the signal magnitude areas of the net effect and the measurable net effect, see Figure 5.3. The depth of burial was defined by the top of the target and

therefore two depth values below zero can be observed in the graph. These correspond to a half submerged and half exposed target and a target lying on top of the seafloor. The measurability curve of the burial depth is used to determine a fit, which is shown as a black line in the chart and is given by:

$$\mathcal{N} = \frac{2.386 \times 10^{-3}}{(d_{\text{target}} + 1.529)^{7.751}} \tag{5.1}$$

The equation for the fitted curve shows that the net effect decreases between the 7^{th} and 8^{th} power for burial depth in metres. The measurability curve in Figure 5.1 becomes a vertical line after a depth of burial of 2 metres. This means that after two metres the value goes to zero and therefore a target of 0.1 by 0.1 by 0.4 metres at more than 2 metres burial depth is not measurable under the assumptions we took in Section 4.3.

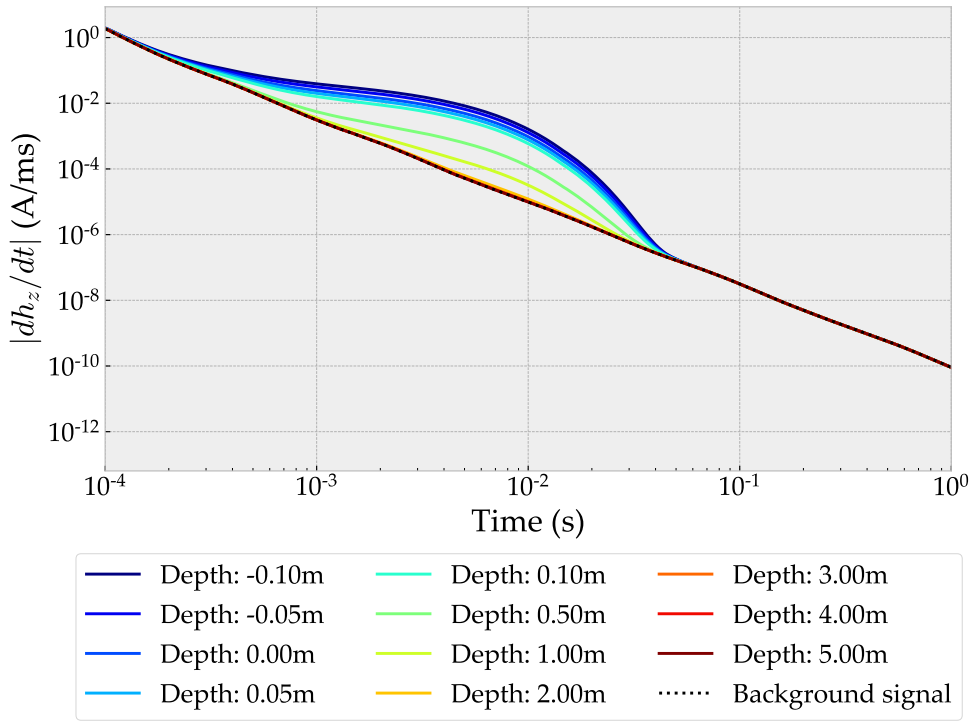

Figure 5.1: Signals computed in one-at-a-time depth of burial analysis.

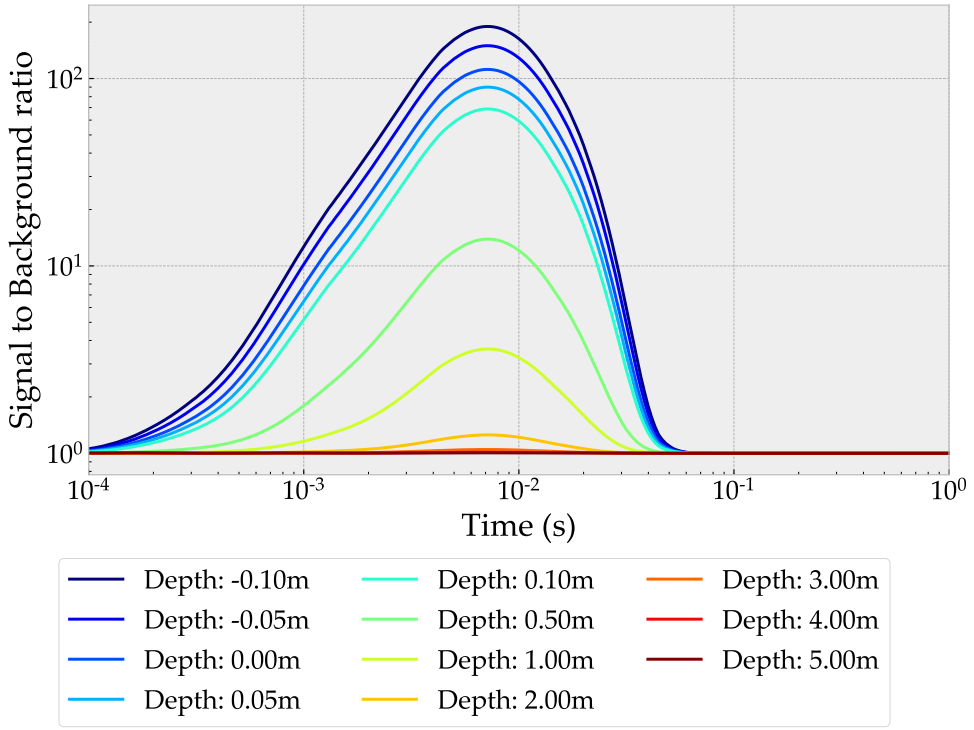

Figure 5.2: Signal to background ratio over time in one-at-a-time depth of burial analysis.

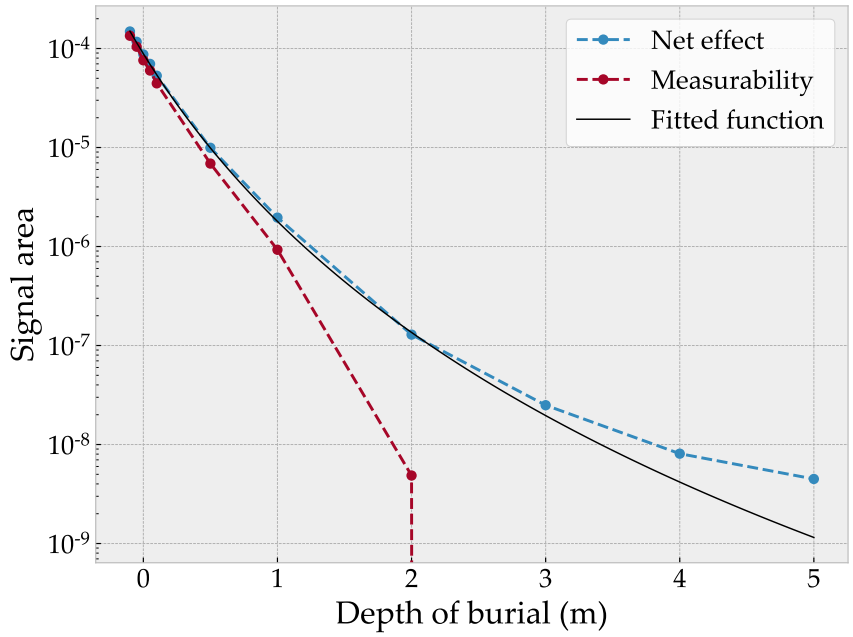

Figure 5.3: Net effect with fit and measurability points for depth of burial experiment.

5.1.2 Size

To analyse the influence of the size of a target on the net effect and measurability we conducted two experiments. The first being the characteristic size experiment, where we compute the response for different characteristic size, which causes change in all three dimensions of the target. The second being the area versus volume experiment, where we start with the same object and generate two curves. One for constant volume and increasing horizontal area, the other for constant horizontal area and increasing volume. We show the results of both experiments in this section.

Characteristic size

In our characteristic size experiments, we compare targets of different sizes at two metres below the seafloor. The size is scaled in all three dimensions of the target and is determined by the characteristic size. The width and height of the target are equal to the characteristic size and the length equals four time the characteristic size. Alike the size experiment, a computed signal chart and a signal to background ratio chart were generated for the characteristic size experiment. They can be found in Appendix C. Here, we show the net effect and measurability curves for characteristic size in Figure 5.4. The net effect is fitted with a polynomial that is given by:

$$\mathcal{N} = (1.024 \times 10^{-4})S_c^3 + (1.862 \times 10^{-5})S_c^2 + (4.794 \times 10^{-7})S_c - 4.978 \times 10^{-8} \tag{5.2}$$

The measurability curve goes to zero for characteristic sizes smaller than 0.1 metres. Consequently, targets smaller than 0.1 by 0.1 by 0.4 metres at two metres burial depth are no longer measurable under the assumptions made in Section 4.3. This is exactly the same observation that we made in the depth of burial experiment.

Area versus volume

Our second experiment regarding the size of the target is the area versus volume experiment. Here we try to find out what determines the response more, the horizontal area or the volume of a target. Starting with exactly the same target, we computed two sets of responses. One with a constant volume and a changing area, and the other with a constant area and changing volume. For both of these sets we computed the net effect, which is shown in Figure 5.5. In this figure, the x-axis denotes the multiplier of the starting target. Going from 1 to 2 means the area is doubled for the constant volume curve (in blue) and means the volume is doubled for the constant area curve (in red). Both curves are fitted with a polynomial. The polynomial fitting the area of the target (A_{target}) to the net effect ($\mathcal{N}$) is given by:

$$\mathcal{N} = (7.696 \times 10^{-11})A_{\text{target}}^3 - (1.897 \times 10^{-9})A_{\text{target}}^2 + (3.02 \times 10^{-8})A_{\text{target}} + 1.227 \times 10^{-8}. \tag{5.3}$$

The polynomial fitting the volume of the target (V_{target}) to the net effect (A) is given by:

$$\mathcal{N} = (2.573 \times 10^{-10})V_{\text{target}}^3 - (4.781 \times 10^{-9})V_{\text{target}}^2 + (3.654 \times 10^{-8})V_{\text{target}} + 8.676 \times 10^{-9}. \tag{5.4}$$

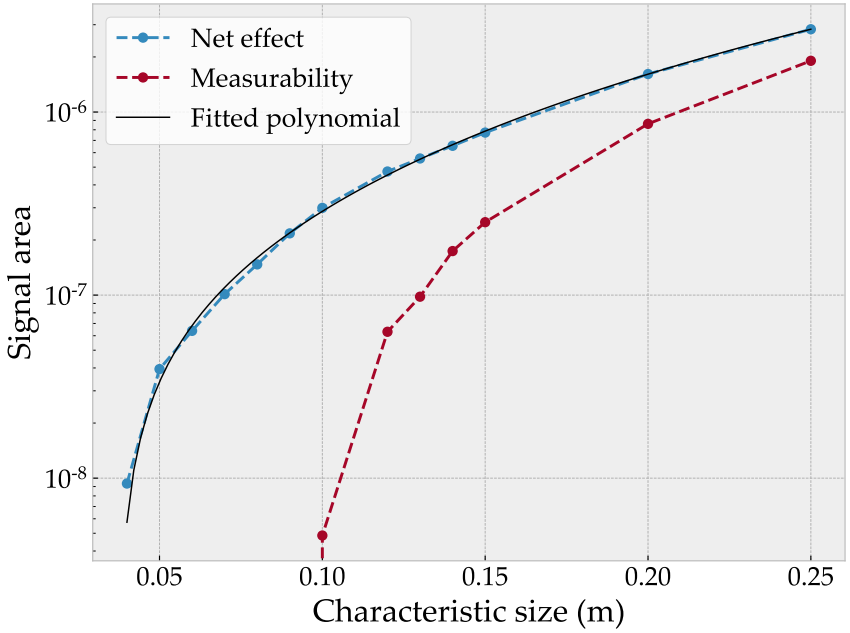

Figure 5.4: Net effect with fit and measurability points for characteristic size experiment.

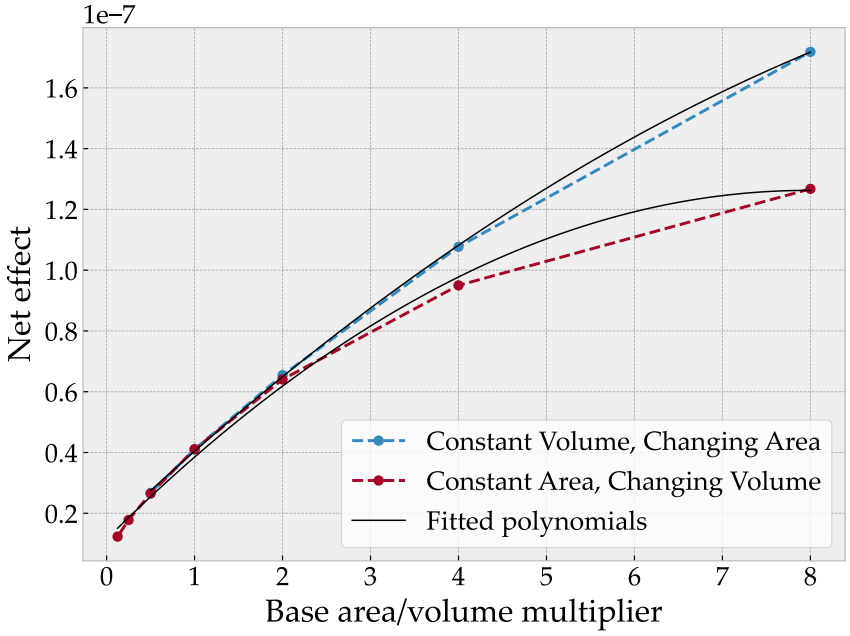

Figure 5.5: Net effect with fitted polynomials for area versus volume experiment.

5.1.3 Wall thickness

The third individual parameter we investigated is the wall thickness (Δx_{wall}). We compute the response for our standard target of 0.1 by 0.1 by 0.4 metres, at 2 metres below the seafloor with a wall thickness ranging from 10 millimetre to 50 millimetres. From the responses and the background response we again computed the net effect and the measurability under the assumptions made in Section 4.3. The net effect and measurability are plotted against the wall thickness in Figure 5.6. The net effect is fitted with a polynomial, which is given by:

$$\mathcal{N} = -(1.863 \times 10^{-8})\Delta x_{\text{wall}}^2 + (1.732 \times 10^{-9})\Delta x_{\text{wall}} + 2.996 \times 10^{-7}. \tag{5.5}$$

The net effect is visually not changing at all in this graph, but it is just slightly increasing for larger thicknesses. The measurability shows a steep increase from a ten millimetre wall to a twenty millimetre wall. This large effect is caused by a part of the signal that is just under the signal noise level in the target with ten millimetre wall thickness and above the signal noise level in the target with twenty millimetre wall thickness. The response itself for ten millimetre wall thickness does not look much different compared to the response for twenty millimetre wall thickness (see Appendix C), just as the net effect describes. This steepness is more nuanced in Figure C-7 in Appendix C by plotting the measurability against the ferrous volume instead of the thickness. The polynomial fit that is used there for the net effect is given by:

$$\mathcal{N} = (5.035 \times 10^{-7})V_{\text{ferrous}}^2 + (7.449 \times 10^{-9})V_{\text{ferrous}} + 2.996 \times 10^{-7}. \tag{5.6}$$

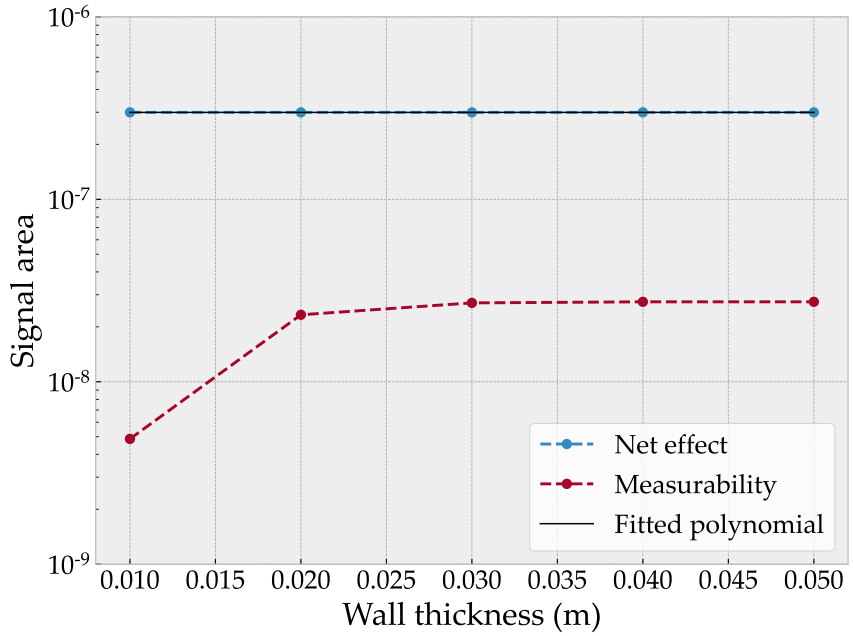

Figure 5.6: Net effect with fit and measurability for thickness experiment.

5.2 Relative significance

To compare the effects that the different parameters have on the signal response we defined a statistical approach in Section 4.4.2 to investigate the relative significance of the parameters. The result of this complete analysis is given in the tornado chart, see Figure 5.7. In this chart the different parameters are plotted against the net effect. The net effect is used, because that gives insight into the exact relation of a parameter and the corresponding target response, whether it is actually measurable or not. The middle line, the boundary between the red and blue bars, is the net effect of the response if all parameters are set to their P50 value. For each parameter, the left boundary of the bar corresponds to the net effect of the response with the parameter set to its P10 value, and all other parameters at their P50 value. Likewise, the right boundary of each bar corresponds to the net effect of the response with that parameter set to its P90 value and all other parameters to its P50 value. In the chart, the parameters are sorted from the largest to the lowest impact on the net effect.

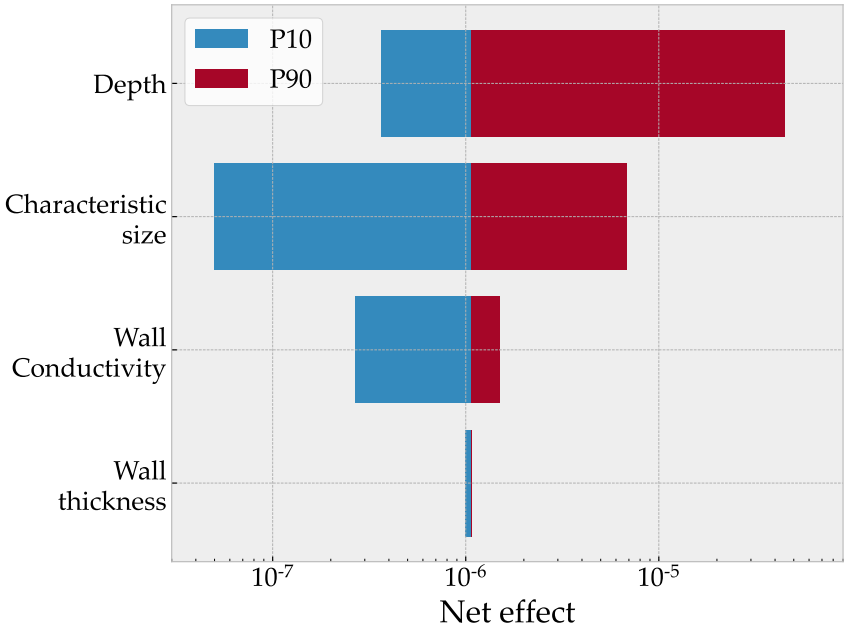

Figure 5.7: Influence of P10 and P90 on the net effect for target parameters.

The tornado chart shows us that the depth and characteristic size have the largest impact on the net effect for the parameter distributions used. The characteristic size also returns the smallest net effect for its P10 value. This means that in the parameter ranges chosen, the characteristic size is the most critical parameter. The values on the lower end of the characteristic size spectrum produce the least net effect and those targets will therefore be the hardest to detect. In line with our findings from Section 5.1 the wall thickness does have much impact. Although more thickness significantly increases the ferrous volume the target response stays almost the same.

5.3 Characterisation experiment

In our characterisation experiment we placed a metal scrap piece on the seafloor and a target below the seafloor to see what the influence of the signal would be. The geometry of this experiment is explained in Section 4.5. In this case, it makes most sense to look at the signal to background ratios. The signal to background ratios for the model with and without scrap piece, and also for only the scrap piece are given in Figure 5.8. Their original signals can be found in Appendix C in Figure C-8.

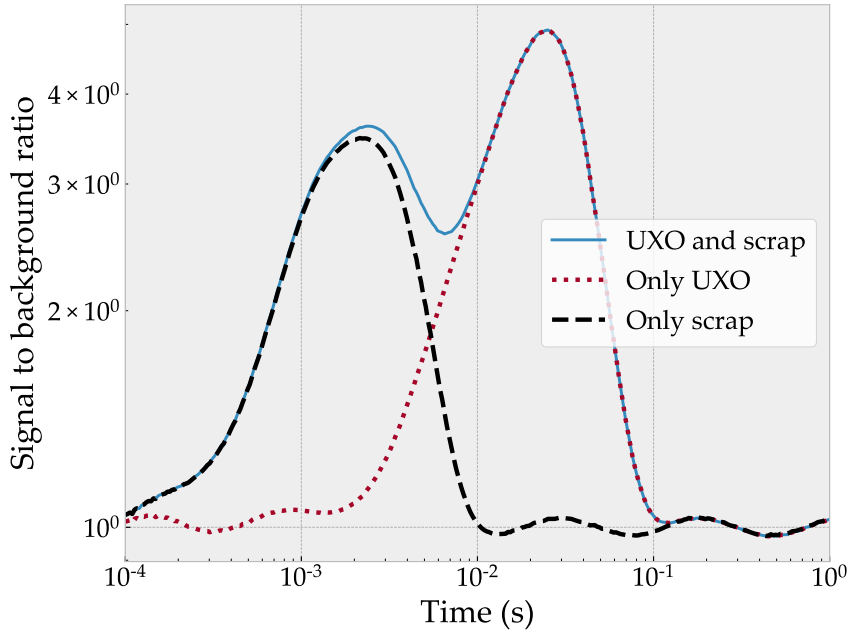

Figure 5.8: Signal to background ratio over time for the curves in the characterisation experiment.

It is very hard to distinguish the response of scrap and the response of a UXO target. In our simulations, where only the z component is recorded, the UXO and the scrap produce very similar shaped responses although their geometry is different. It is possible to distinguish between a deeper and a lower target based on the time of their response, but then it still remains a question what the object actually is. In Figure 5.8 the response of the scrap on the seafloor is not noticeable anymore after 10 ms. The signal to background ratio of the simulated UXO and scrap response is visually not different than the signal to background ratio of only the UXO piece.

5.4 Discussion

We showed the results for individual parameters, relative significance, and the characterisation experiment. We discuss the outcomes of these three subjects in this section. Our main findings for the individual parameter sensitivity analysis are:

- The total net effect decreases between the 7^{th} and 8^{th} power with increasing burial depth in metres. We determined this power by fitting a function to the net effect values for the investigated burial depths. This means the burial depth is a very sensitive parameter to UXO detection, as deeper targets produce significantly less signal.
- The increase of net effect with specific size of a target can be approximated with a cubic polynomial. The increase of net effect with target volume and the increase of net effect with horizontal area of the target, can both also be approximated with cubic polynomials.
- The horizontal oriented area of the target is the most dominant size parameter, because in the area versus volume experiment the curve corresponding to increasing area has a steeper slope than the curve corresponding to increasing volume.
- A conductor of 0.1 by 0.1 by 0.4 metres or smaller, buried more than 2 metres under the seafloor, with a wall thickness of 0.01 metre, is no longer measurable under our measurability assumptions. This means that a same sized target, which is buried at two metres depth or less, is measurable. We do not claim that there are no targets measurable at all deeper than 2 metres under the seafloor. Despite the fact that more burial depth decreases the response between the 7^{th} and 8^{th} power, larger targets increase the response. Thus, targets larger than 0.1 by 0.1 by 0.4 metres can be measurable at more than 2 metres depth. Further research is needed to determine the combined effects of depth and size of a target on the net effect.
- Although a thicker target wall adds conductive volume to the target, it has no significant impact on the response. This means the 0.01 metre wall thickness can already maintain the eddy current. That the net effect is almost not increasing with more ferrous volume is contradicting to the one-at-a-time size experiments, where extra volume does significantly increase the response. This is the case, because in size experiments extra volume is added by making the outer dimensions of the target larger, and in the thickness experiment extra volume is added by making the wall thickness larger.

Our main findings for the relative significance experiment are:

- From most significant to least significant parameter: burial depth, characteristic size, wall conductivity and wall thickness. This can be deducted from the tornado chart presented in Figure 5.7 by the length of the bars.
- The result of this approach would be most useful when computed for real data, see the paragraph on the next page called 'statistical approach'.

Our main findings for the characterisation experiment are:

- Metal scrap produces responses very much alike UXO responses. More research is needed to determine how these signals can be characterised, see the paragraph on the next page called 'three dimensional receiver antennas'.

Noise assumptions

Another point of discussion is also coupled to real life experiments. To determine which part of the net effect could be accounted as measurability, we took assumptions about the noise based on literature. When one would want to determine the relations between target parameters and net effect of the response, such as we did, it would be best to determine these noise assumptions in a practical experiment for the sensor that will be used.

Late time error

The main uncertainty of all our simulations lies in the error in the SimPEG simulations that could not be overcome. In the software validation (Chapter 3) an inevitable error that would increase with time was found. For the loop source this error was 14 percent or lower. This error was visible in all signals and would therefore not corrupt the net effect computations immediately. In the software validation we used a cylindrical mesh and could therefore discretise the problem finer with less cells, compared to the three-dimensional mesh used for the simulations defined in Chapter 4. In the simulations of our sensitivity analysis this same error was present. This adds an uncertainty to our results, although this is minimised by comparing the differences between signals, because those signals have the same error. This could be overcome by implementing a higher order time stepping scheme in SimPEG, which currently uses a first order backward Euler scheme.

Computational cost

We have determined relations between target parameters in the marine model and the net effect. These relations are valid for variation of one parameter and with standard values for other parameters. In order to determine a relation in which all the parameters would be included, more simulations are needed to sample this multi-dimensional parameter space. In our approach this would require much more computational cost.

Statistical approach

It is hard to deduce conclusions from the results of the statistical approach. The problem lies in the parameter distributions. Although they are not unrealistic, they are arbitrary. Applying this approach on a real site where an initial investigation already took place would make more sense. The statistical approach would then lead to findings that would be of direct use.

Three dimensional receiver antennas

The characterisation experiment we carried out is very limited, but it does show us that characterisation between a piece of scrap and a UXO can be very difficult. To make the characterisation process less arbitrary, three component receivers should be added for more information. With the three components polarisabilities of an object can be computed, which can be used to match the signals to a UXO model, see for example Pasion and Oldenburg (2001).

6 | Conclusion

The principal aim of this research was to determine under which conditions we can detect a conductor on or below the seafloor using a time domain loop source. To answer this question the responses of conductors under different conditions were modelled and analysed.

To model the TEM responses we used the Python package SimPEG. Before we would use it to compute the marine TEM responses, we put the package to the test. We computed responses with SimPEG that we compared with analytical equations from Ward and Hohmann (1988). We found that we could model the derivative of the magnetic field from a loop source with an error of 14 percent or lower. This is quite significant, but because the same error shows up in all modelled signals, we settled with it.

Then, we introduced two quantities to compare multiple signals with each other, the net effect and the measurability. The net effect we defined as the area between a signal, acquired on sensing on a target, and the background response. This is an integration of all the signal added by a target over the background response. In reality, this cannot be measured exactly and therefore we came up with the measurability. The measurability we defined as the net effect area limited by three constraints: the time resolution, the noise level, and the signal noise including effects of the (moving) water. Based on literature and previous experiments we made assumptions regarding these three constraints.

With our software tested and criteria to compare responses in place, we were ready to approach the main problem of this thesis. We introduced a marine model with a conductor below the seafloor and a source and receiver right above it. The conductor is a hollow cuboid with a conducting wall and a resisting interior, a rectangular approximate of an UXO piece. Then, we defined two approaches to investigate under which conditions we can detect a conductor on the seafloor.

In the first approach, we focused on the influences on the net effect and measurability, when changing a single parameter while keeping all the others constant. The parameters we investigated using this approach were the burial depth, size, and wall thickness of the conductor. For the other parameters we defined a standard situation and kept them in that setting. Our main findings here were:

- The total net effect decreases between the 7^{th} and 8^{th} power with increasing burial depth in metres.

- The increase of net effect with specific size of a target can be approximated with a cubic polynomial.
- The horizontal oriented area of the target is the most dominant size parameter.
- A conductor of 0.1 by 0.1 by 0.4 metres or smaller, buried more than 2 metres under the seafloor is no longer measurable under our measurability assumptions.
- Although a thicker target wall adds conductive volume to the target, it has no significant impact on the response.

In our second approach, we focused on the relative significance of the parameters: burial depth, characteristic size, wall conductivity and wall thickness. We created value distributions for these parameters and computed the responses for each parameter at their 10^{th} and 90^{th} percentile and the other parameters at their median. From these computations we created a tornado chart showing off the relative significance of these parameters. Our main findings were:

- From most significant to least significant parameter: burial depth, characteristic size, wall conductivity and wall thickness.
- The result of this approach would be most useful when computed for real data.

The two approaches together showed us that time domain electromagnetic loop sources can be used to detect conductors on the seafloor, but their responses become too small to measure for objects smaller than 0.1 by 0.1 by 0.4 metres at more than 2 metres below the seafloor.

References

Auken, E., Foged, N., Larsen, J. J., Lassen, K. V. T., Maurya, P. K., Dath, S. M., & Eiskjær, T. T. (2019). tTEM—A towed transient electromagnetic system for detailed 3D imaging of the top 70 m of the subsurface. *Geophysics*, *84*(1), E13–E22.

Billings, S. D. (2004). Discrimination and classification of buried unexploded ordnance using magnetometry. *IEEE Transactions on Geoscience and Remote Sensing*, *42*(6), 1241-1251.

Castillo-Reyes, O., de la Puente, J., & Cela, J. M. (2018). PETGEM: A parallel code for 3D CSEM forward modeling using edge finite elements. *Computers & Geosciences*, *119*, 123–136.

Chu, P. C., Fan, C., & Gefken, P. R. (2008). Semi-empirical formulas of drag/lift coefficients for high-speed rigid body maneuvering in water column. *Adv. Fluid Mech*, *7*, 163–172.

Cockett, R., Kang, S., Heagy, L. J., Pidlisecky, A., & Oldenburg, D. W. (2015). SimPEG: An open source framework for simulation and gradient based parameter estimation in geophysical applications. *Computers & Geosciences*, *85*, 142–154.

Constable, S. (2010). Ten years of marine CSEM for hydrocarbon exploration. *Geophysics*, *75*(5), 75A67–75A81.

Diebel, J. (2006). Representing attitude: Euler angles, unit quaternions, and rotation vectors. *Matrix*, *58*(15-16), 1–35.

Doll, W. E., Gamey, T. J., Holladay, J. S., Sheehan, J. R., Norton, J., Beard, L. P., … Lahti, R. M. (2010). Results of a high-resolution airborne TEM system demonstration for unexploded ordnance detection. *Geophysics*, *75*(6), B211–B220.

EM61MK2 operating instructions (2.15 ed.) [Computer software manual]. (2011, 8). 1745 Meyerside Drive, Mississauga, Ontario, Canada.

Haber, E. (2014). *Computational methods in geophysical electromagnetics* (Vol. 1). SIAM.

Heagy, L. J., Cockett, R., Kang, S., Rosenkjaer, G. K., & Oldenburg, D. W. (2017). A framework for simulation and inversion in electromagnetics. *Computers & Geosciences*, *107*, 1–19.

Heagy, L. J., Cockett, R., Oldenburg, D. W., & Wilt, M. e. a. (2015). Modelling electromagnetic problems in the presence of cased wells. In *2015 SEG Annual Meeting*.

Hunziker, J., Thorbecke, J., & Slob, E. (2015). The electromagnetic response in a layered vertical transverse isotropic medium: A new look at an old problem. *Geophysics*, *80*(1), F1–F18.

Hyman, J. M., & Shashkov, M. (1999). Mimetic discretizations for Maxwell's equations. *Journal of Computational Physics*, *151*(2), 881–909.

Jenkins, S. A., Inman, D. L., Richardson, M. D., Wever, T. F., & Wasyl, J. (2007, Jan). Scour and Burial Mechanics of Objects in the Nearshore. *IEEE Journal of Oceanic Engineering*, *32*(1), 78-90.

Kaufman, A. A., & Keller, G. V. e. a. (1983). *Frequency and transient soundings* (R. S. Chi-Yu King, Ed.). Elsevier Science Publ. Co., Inc.

Key, K. (2012). Is the fast Hankel transform faster than quadrature? *Geophysics*, *77*(3), F21–F30.

Landmine Monitor 2019: 21st annual edition. (2019). International Campaign to Ban Land Mines, Human Rights Watch.

Li, Y.-G., & Constable, S. (2010). Transient electromagnetic in shallow water: insights from 1D modeling. *Chinese Journal of Geophysics*, *53*(3), 737–742.

Lorrain, P., & Corson, D. R. (1970). *Electromagnetic Fields and Waves* (2nd ed.). San Francisco, California (USA): WH Freeman.

MacInnes, S. C., Snyder, D. D., & Zonge, K. L. (2002). *Physics-Based Characterization of UXO from Multi-Component TEM Data* (Tech. Rep.). 3322 E Fort Lowell Rd, Tucson, AZ 85716 (USA): Zonge Engineering & Research Organization.

Myer, D., Constable, S., Key, K., Glinsky, M. E., & Liu, G. (2012). Marine CSEM of the Scarborough gas field, Part 1: Experimental design and data uncertainty. *Geophysics*, *77*(4), E281–E299.

Nabighian, M. N. (1991). *Electromagnetic Methods in Applied Geophysics: Volume 1, Theory*. Society of Exploration Geophysicists.

Naval Ordnance Systems Command. (1946). *British Explosive Ordnance* (Tech. Rep.). Washington DC (USA): Navy Department. Bureau of Ordnance.

O'Neill, K. A. (2016). *Discrimination of subsurface unexploded ordnance* (1st ed.). Bellingham, Washington (USA): SPIE Press.

Palacky, G. (1988). Resistivity characteristics of geologic targets. *Electromagnetic methods in applied geophysics*, *1*, 53–129.

Pasion, L. R. (2007). *Inversion of time domain electromagnetic data for the detection of unexploded ordnance* (Unpublished doctoral dissertation). University of British Columbia.

Pasion, L. R., & Oldenburg, D. W. (2001). A discrimination algorithm for UXO using time domain electromagnetics. *Journal of Environmental & Engineering Geophysics*, *6*(2), 91–102.

Pavlov, D. A., & Zhdanov, M. S. (2001). Analysis and interpretation of anomalous conductivity and magnetic permeability effects in time domain electromagnetic data: Part I: Numerical modeling. *Journal of Applied Geophysics*, *46*(4), 217 - 233.

Prouty, M., George, D. C., & Snyder, D. D. (2011). *Metalmapper: A multi-sensor TEM system for UXO detection and classification* (Tech. Rep.). 2190 Fortune Dr, San Jose, CA 95131 (USA): Geometrics Inc.

Rice, J. A. (2006). *Mathematical statistics and data analysis*. Cengage Learning.

Rochlitz, R., Skibbe, N., & Günther, T. (2019). custEM: Customizable finite-element simulation of complex controlled-source electromagnetic data. *Geophysics*, *84*(2), F17–F33.

Salem, A., Hamada, T., Asahina, J. K., & Ushijima, K. (2005). Detection of unexploded ordnance (UXO) using marine magnetic gradiometer data. *Exploration Geophysics*, *36*(1), 97–103.

Sato, M., Fujiwara, J., Feng, X., Zhou, Z.-S., & Kobayashi, T. (2005). Development of a hand-held GPR MD sensor system (ALIS). In *Detection and remediation technologies for mines and minelike targets x* (Vol. 5794, pp. 1000–1007).

Saville, S., Bancroft, S., Bell, T., Odlum, N., & Steinhurst, D. (2018). *Underwater advanced time-domain electromagnetic system* (Tech. Rep.). 2411 Dulles Corner

Park, Suite 500, Herndon, Virginia 20171 (USA): CH2M Herndon United States.

Schuddinck, K., & van den Berg, E. (2017). *Site Data Hollandse Kust (noord) Wind Farm Zone* (Tech. Rep.). Alphenseweg 4A, 5133 NE Riel (The Netherlands): REASeuro.

Shubitidze, F., Fernández, J. P., Barrowes, B. E., Shamatava, I., Bijamov, A., O'Neill, K., & Karkashadze, D. (2013). The orthonormalized volume magnetic source model for discrimination of unexploded ordnance. *IEEE Transactions on Geoscience and Remote Sensing*, *52*(8), 4658–4670.

Vuik, C., Vermolen, F. J., Gijzen, M. B., & Vuik, M. (2007). *Numerical Methods for Ordinary differential equations*. VSSD.

Ward, S. H., & Hohmann, G. W. (1988). Electromagnetic theory for geophysical applications. In *Electromagnetic methods in applied geophysics: Volume 1, theory* (pp. 130–311). Society of Exploration Geophysicists.

Werthmüller, D. (2017). An open-source full 3d electromagnetic modeler for 1D VTI media in python: empymod. *Geophysics*, *82*(6), WB9–WB19.

Werthmüller, D., Mulder, W., & Slob, E. (2019). emg3d: A multigrid solver for 3D electromagnetic diffusion. *Journal of Open Source Software*, *4*(39), 1463.

Whittall, K. P., & Oldenburg, D. W. (1992). *Inversion of magnetotelluric data for a one-dimensional conductivity*. Society of Exploration Geophysicists.

Yee, K. (1966). Numerical solution of initial boundary value problems involving Maxwell's equations in isotropic media. *IEEE Transactions on antennas and propagation*, *14*(3), 302–307.

Zhang, Y., Collins, L., Yu, H., Baum, C. E., & Carin, L. (2003). Sensing of unexploded ordnance with magnetometer and induction data: Theory and signal processing. *IEEE Transactions on Geoscience and Remote Sensing*, *41*(5), 1005–1015.

Ziolkowski, A., & Slob, E. (2019). *Introduction to Controlled-source Electromagnetic Methods: Detecting Subsurface Fluids*. Cambridge University Press.

Appendix A

EM equation derivations

We start with Faraday's law (Equation 2.3) and Ampère's law with Maxwell's addition (Equation 2.4):

$$\nabla \times \mathbf{e} + \frac{\partial \mathbf{b}}{\partial t} = -\mathbf{j}^{\mathbf{m}}, \tag{A-1}$$

$$-\nabla \times \mathbf{h} + \frac{\partial \mathbf{d}}{\partial t} + \mathbf{j} = -\mathbf{j}^{\mathbf{e}}. \tag{A-2}$$

If we assume the physical properties are homogeneous throughout the domain and substitute the constitutive relations $\mathbf{b} = \mu\mathbf{h}$, $\mathbf{d} = \epsilon\mathbf{e}$, and $\mathbf{j} = \sigma\mathbf{e}$ we obtain:

$$\nabla \times \mathbf{e} + \mu\frac{\partial \mathbf{h}}{\partial t} = -\mathbf{j}^{\mathbf{m}}, \tag{A-3}$$

$$-\nabla \times \mathbf{h} + \epsilon\frac{\partial \mathbf{e}}{\partial t} + \sigma\mathbf{e} = -\mathbf{j}^{\mathbf{e}}. \tag{A-4}$$

Under the diffusive approximation the term with ϵ vanishes and we end up with:

$$\nabla \times \mathbf{e} + \mu\frac{\partial \mathbf{h}}{\partial t} = -\mathbf{j}^{\mathbf{m}}, \tag{A-5}$$

$$-\nabla \times \mathbf{h} + \sigma\mathbf{e} = -\mathbf{j}^{\mathbf{e}}. \tag{A-6}$$

From these two equations we can isolate $\frac{\partial \mathbf{h}}{\partial t}$ and $\mathbf{e}$ as follows:

$$\frac{\partial \mathbf{h}}{\partial t} = -\mu^{-1}\mathbf{j}^{\mathbf{m}} - \mu^{-1}\nabla \times \mathbf{e}, \tag{A-7}$$

$$\mathbf{e} = \sigma^{-1}\nabla \times \mathbf{h} - \sigma^{-1}\mathbf{j}^{\mathbf{e}}. \tag{A-8}$$

To substitute these expressions, we first have to take the time derivative of Equation A-6, which yields:

$$-\nabla \times \frac{\partial \mathbf{h}}{\partial t} + \sigma\frac{\partial \mathbf{e}}{\partial t} = -\frac{\partial \mathbf{j}^{\mathbf{e}}}{\partial t}. \tag{A-9}$$

Now we can fill in the isolated expressions for $\mathbf{e}$ and $\frac{\partial \mathbf{h}}{\partial t}$ into respectively Equation A-5 and Equation A-9, and move the source terms to the right hand side to end up with the final expressions:

$$\nabla \times \mu^{-1} \nabla \times \mathbf{e} + \sigma \frac{\partial \mathbf{e}}{\partial t} = -\nabla \times \mu^{-1} \mathbf{j}^{\mathbf{m}} - \frac{\partial \mathbf{j}^{\mathbf{e}}}{\partial t}, \tag{A-10}$$

$$\nabla \times \sigma^{-1} \nabla \times \mathbf{h} + \mu \frac{\partial \mathbf{h}}{\partial t} = \nabla \times \sigma^{-1} \mathbf{j}^{\mathbf{e}} - \mathbf{j}^{\mathbf{m}}. \tag{A-11}$$

Appendix B

Mesh characteristics

Table B-1: Mesh characteristics for simulated problems

Problem	**Mesh type**	**No. of core cells**	**Core cell size**	**No. of padding cells**	**Expansion factor**	**Total no. of cells**
Dipole	Cylindrical	150	1	60	1.3	
Loop	Cylindrical	40	3	30	1.3	
Receiver array	Cylindrical	600	3	100	1.2	
Object rotation	Tensor	31 (x,y) 30 (z)	0.1 (x,y) 0.1 (z)	17	1.9	270.400

Appendix C

Additional figures

In this appendix additional figures of the following experiments can be found:

- Empymod versus analytics
- Characteristic size experiment
- Thickness experiment
- Characterisation experiment

Empymod versus analytics

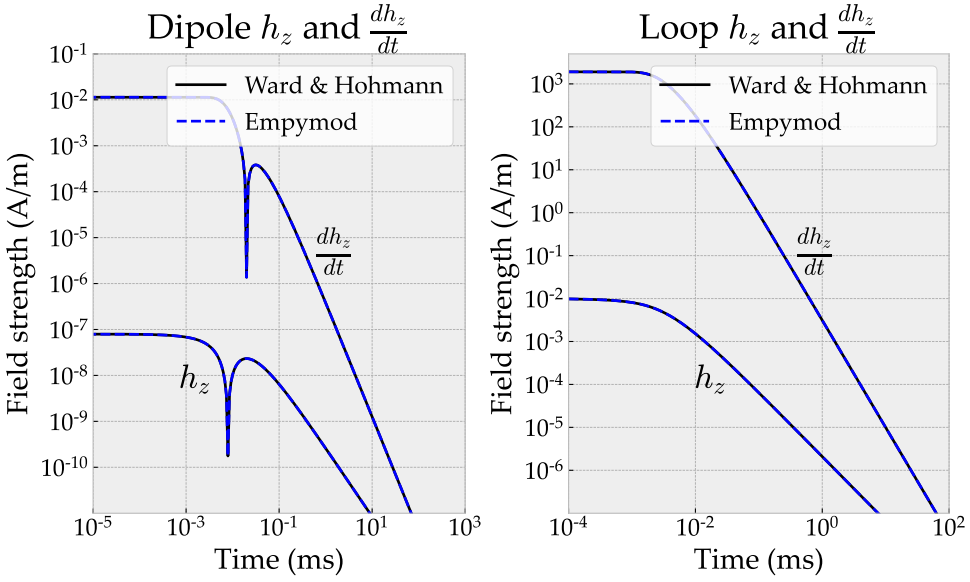

(**a**) Dipole source and point receiver. (**b**) Loop source and point receiver.

Figure C-1: Empymod results compared with analytic solutions. Both are absolute values.

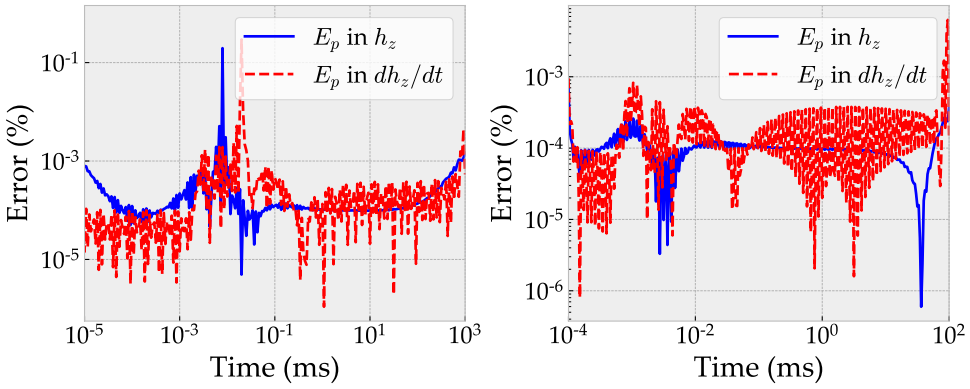

(**a**) Dipole source and point receiver. (**b**) Loop source and point receiver.

Figure C-2: Percent errors between empymod simulations and analytical solutions.

Characteristic size experiment

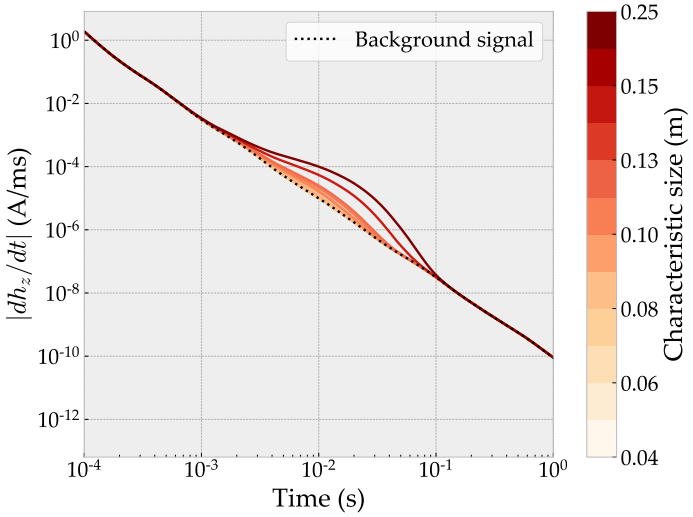

Figure C-3: Signals computed in one-at-a-time size analysis.

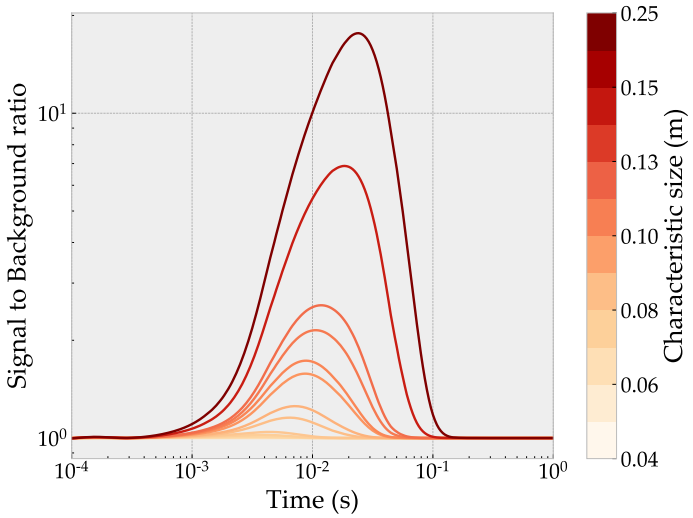

Figure C-4: Signal to background ratio over time in one-at-a-time size analysis.

Thickness experiment

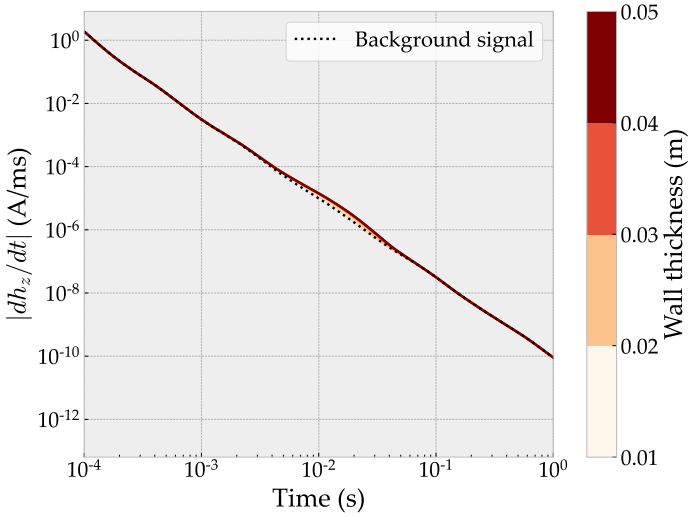

Figure C-5: Signals computed in one-at-a-time thickness analysis.

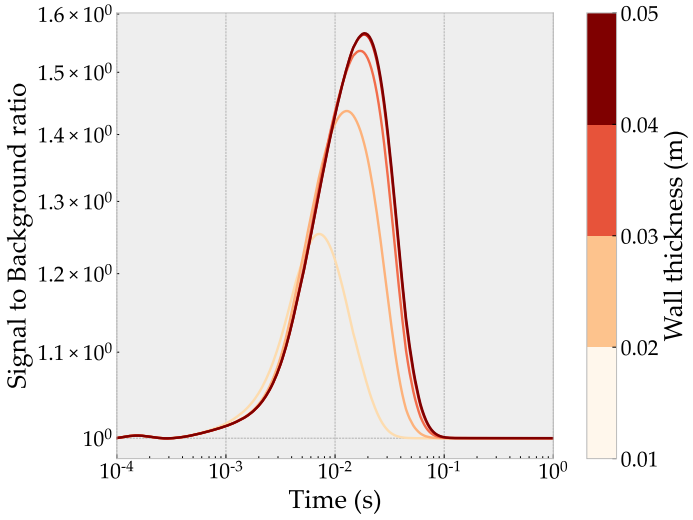

Figure C-6: Signal to background ratio over time in one-at-a-time thickness analysis.

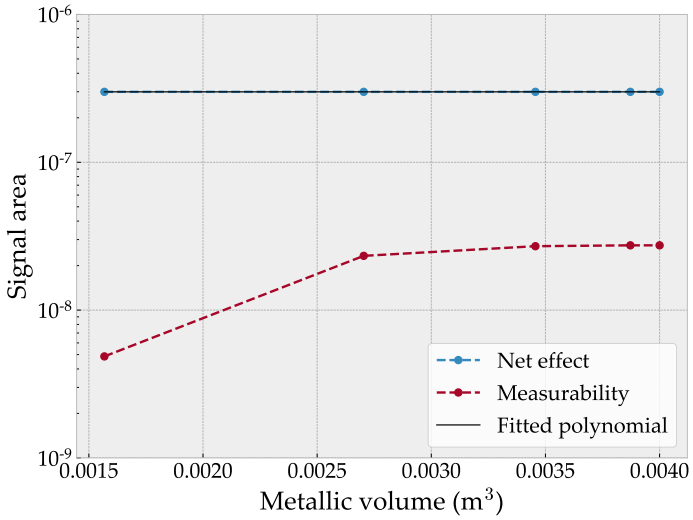

Figure C-7: Net effect with fit and measurability for thickness experiment.

Characterisation experiment

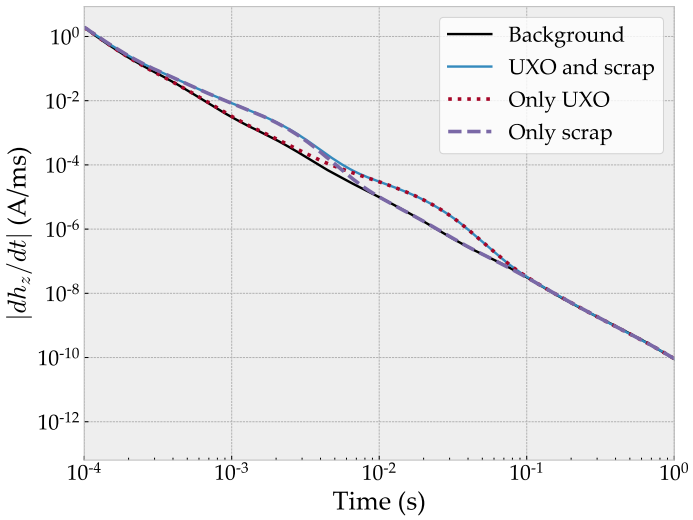

Figure C-8: Computed signals in the characterisation experiment.

Appendix D

Rotation experiment

In this experiment we review a land based setting with a conducting object located in the subsurface. We consider the most common acquisition setup, the loop. We combine this with a point receiver at the centre of the loop. A common example of a TDEM loop-loop system is the EM61-MK2A. This is a wheel cart consisting of two coaxial rectangular coils. One being the EM source and the main coincident EM receiver, and the other being the secondary EM receiver, which is used for focusing. The system measures four user-specified time gates ("EM61MK2 Operating Instructions", 2011). The setup we use in this chapter behaves similarly to the EM61-MK2A.

Land model

The model we use in this section is a simplified earth. This simplified earth is built in a three-dimensional Cartesian coordinate system with the positive z axis pointing downwards. It is built from two semi-infinite half-spaces interfacing at $z = 0$. The bottom ($z > 0$) semi-infinite half-space is homogeneous and isotropic soil. On top of this is another semi-infinite half-space of air, which is also homogeneous and isotropic. As a consequence, the electrical resistivity in both half-spaces is uniform. In addition there is a rectangular box located at $(x, y, z) = (0, 0, d_{\text{box}})$. This box has a length L of three metres, a width W and height H of fifty centimetres, has its own resistivity value ρ_{box}, and its own permeability value μ_{box}. The box can be interpreted as a simplification of an UXO piece.

The box can be rotated about axis z, y, and x with angles α, β, and γ. These angles are Tait-Bryan angles and the rotation is intrinsic. In aviation, α, β, and γ are known as yaw, pitch and roll. Rotation of the box vertices is computed with Equation D-1. In this equation x', y', and z' are the rotated x, y, and z coordinates of the vertices. The rotation matrix R is given in Equation D-2 (Diebel, 2006).

$$\begin{pmatrix} x' \\ y' \\ z' \end{pmatrix} = R(\alpha, \beta, \gamma) * \begin{pmatrix} x \\ y \\ z \end{pmatrix}. \tag{D-1}$$

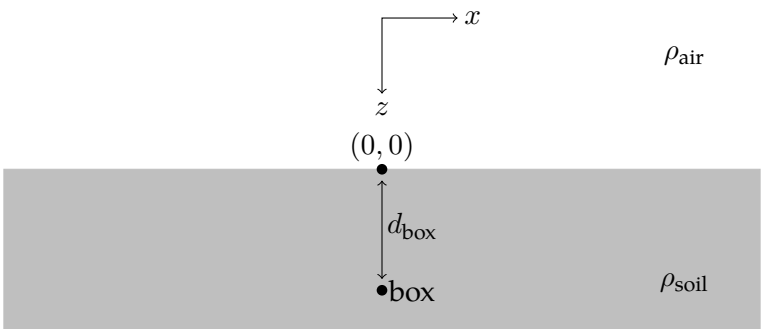

Figure D-1: The half-space earth of the land problem. ρ_{air} and ρ_{soil} are the air resistivity and the soils resistivity, respectively.

$$R = R_z(\alpha)R_y(\beta)R_x(\gamma) = \begin{bmatrix} \cos\alpha & -\sin\alpha & 0 \\ \sin\alpha & \cos\alpha & 0 \\ 0 & 0 & 1 \end{bmatrix} \begin{bmatrix} \cos\beta & 0 & \sin\beta \\ 0 & 1 & 0 \\ -\sin\beta & 0 & \cos\beta \end{bmatrix} \begin{bmatrix} 1 & 0 & 0 \\ 0 & \cos\gamma & -\sin\gamma \\ 0 & \sin\gamma & \cos\gamma \end{bmatrix}$$

$$R = \begin{bmatrix} \cos\alpha\cos\beta & \cos\alpha\sin\beta\sin\gamma - \sin\alpha\cos\gamma & \cos\alpha\sin\beta\cos\gamma + \sin\alpha\sin\gamma \\ \sin\alpha\cos\beta & \sin\alpha\sin\beta\sin\gamma + \cos\alpha\cos\gamma & \sin\alpha\sin\beta\cos\gamma - \cos\alpha\sin\gamma \\ -\sin\beta & \cos\beta\sin\gamma & \cos\beta\cos\gamma \end{bmatrix}. \tag{D-2}$$

Simulation setup

On the model described in the previous section, we use a standard 1 metre radius horizontal loop source with its centre at $(x, y, z) = (0, 0, 0)$. The receiver is modelled as a point at $(x, y, z) = (0, 0, 0)$ and measures the the dh_z/dt signal, which would be normally measured by a receiver loop. Four different tests are modelled. One where the brick is aligned with the numerical spatial grid, and three where the brick is rotated and not aligned with the numerical spatial grid. In Table D-1 the changing parameters for the tests are given. What changes in these tests are the rotations yaw and pitch of the object. The yaw is defined as the rotation around the z axis and the pitch is defined as the rotation around the y axis. In Table D-2 the standard parameter values used by all tests.

In comparison to the experiments in the previous chapter, the geometry of this setup is more difficult. It no longer has cylindrical symmetry. Thus, the spatial discretisation in SimPEG requires the use of the three-dimensional tensor mesh. The three-dimensional tensor mesh uses quite a lot of cells more than the cylindrical mesh used in the previous chapter and therefore is computationally more expensive. If one wants to discretise a three-dimensional ten by ten by ten homogeneous model into one by one by one cells, the full three-dimensional tensor mesh would need 1.000 cells, where as the cylindrical mesh would only need 50 cells. The mesh properties we used for this particular simulation can be found in Table B-1 in Appendix B.

The smallest cells used in the mesh were of size 0.1 metre in all three directions (i.e. a ten

Table D-1: Rotational impact tests.

Test #	Yaw (α)	Pitch (β)	Box volume
1	0 °	0 °	0.7250 (m^3)
2	15 °	15 °	0.7402 (m^3)
3	30 °	30 °	0.7574 (m^3)
4	45 °	45 °	0.7248 (m^3)
5	15 °	0 °	0.7350 (m^3)
6	30 °	0 °	0.7500 (m^3)
7	45 °	0 °	0.7550 (m^3)

Table D-2: Standard parameter values rotational tests.

Parameter	Symbol	Value	Unit
Air resistivity	ρ_{air}	10^8	$\Omega\,m$
Soil resistivity	ρ_{soil}	10	$\Omega\,m$
Box resistivity	ρ_{box}	10^{-5}	$\Omega\,m$
Box depth	d_{box}	2.25	m
Box length	L	3	m
Box width	W	0.5	m
Box height	H	0.5	m

centimetre cube). In the objects initial rotation ($\alpha = \beta = 0$) the object is aligned with the mesh cells in the smallest part of the mesh. As the rotational parameters change the spatial discretisation of the object can no longer be perfect. Due to the rectangular mesh cells, the object will not have smooth edges, but the object will have aliased edges. Therefore the discretised volume might also not be the same for rotated objects. In fact, for higher rotational angles, the aliasing objects becomes more aliased and error in the discretised volume greater. The actual discretised volumes for each test can be found in the last column of Table D-1.

Results

For each of the tests with two rotations (test 2-4) the simulated data is visualised in Figure D-2a together with the background signal and the signal of the non-rotated object (test 1). The tests with only yaw rotations are given in Figure D-2b, also with the background signal and the signal of the non-rotated object. For both figures the background signal is given twice, one simulated solution and one semi-analytical solution computed with empymod. Just as in the previous chapter, there is an error in the results simulated with SimPEG. It appears as a small time shift in the graph between the two background signals. This error is the same for all simulations and therefore the comparison between the different simulations is still of value.

What we conclude from the figure, is that the signal becomes stronger for more pitch rotation and arrives earlier. The rotation experiments with only yaw rotation show for the eye all the same curve. All signals follow the same shaped curve as the non-rotated signal and start and end perfectly on the with SimPEG simulated background signal. There is no drastic change when increasing the rotational parameters, the behaviour of the curve is similar, only the signal strength is greater when the pitch is increased. When only the yaw is increased, the signals are almost identical. For every test we computed the detectable area between the object signal and the background signal with Equation 4.7. The results of these computations are given, along with a linear fit in Figure D-3.

The increase in rotation causes the object to be partly closer to the source and receiver combination and partly further away. As the strength of the magnetic field excited by the object decays

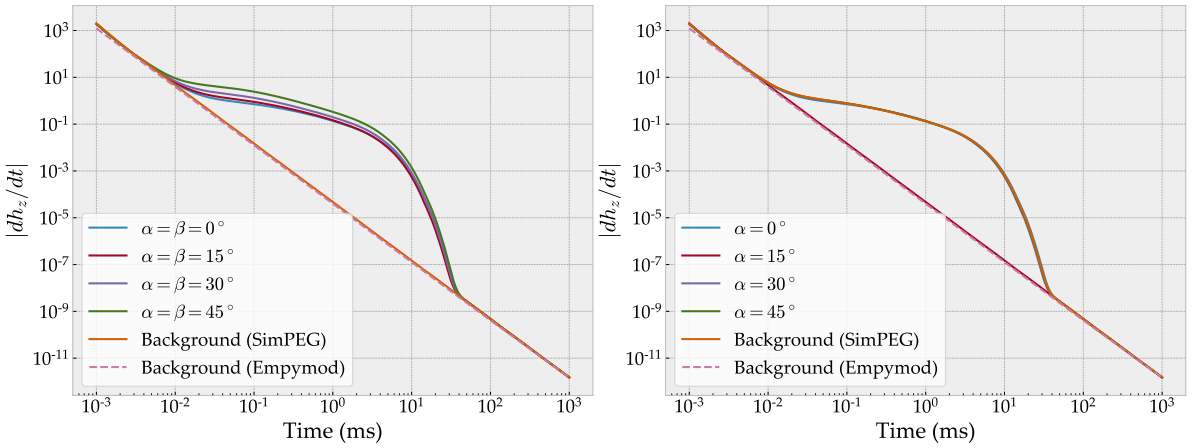

(**a**) Yaw and pitch rotations

(**b**) Only yaw rotations

Figure D-2: Responses for rotated objects

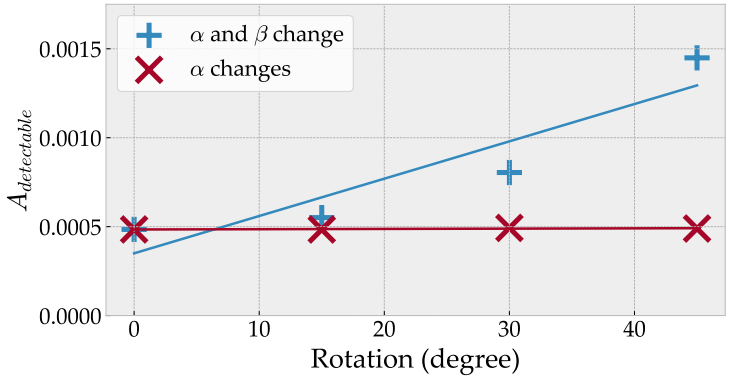

Figure D-3: Detectable area behind rotational experiments with linear fit lines. In red: only yaw rotations. In blue: yaw and pitch rotations.

rapidly with distance, a partly closer and partly further away object results in a higher signal strength, because the closer part of the object weighs more. For our further simulations we make the assumption that rotations of the object are no sensitive parameters to our simulations. The objects depth or conductivity will have a much greater effect on the measured signal. Thus, we can keep objects perfectly aligned with the mesh cells and do not have to take care of aliasing of the object in the spatial discretisation. A small side note to this assumption is the fact that we can still rotate the object with 90 degrees or multiples of 90 for all three rotation angles. These rotations will keep the object aligned with the mesh.

Appendix E

Parameter distributions

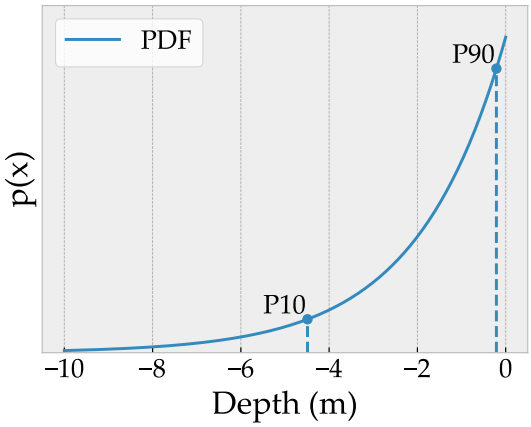

Figure E-1: Probability density function for the target's depth.

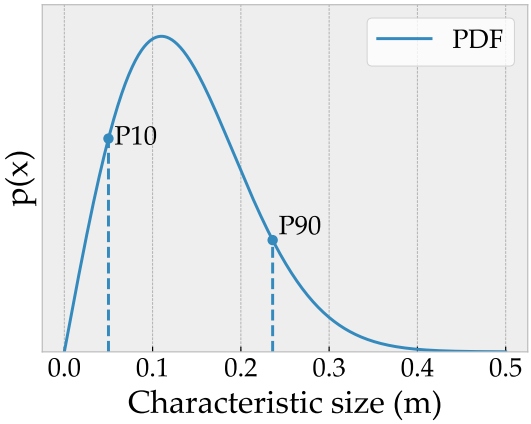

Figure E-2: Probability density function for the target's characteristic size.

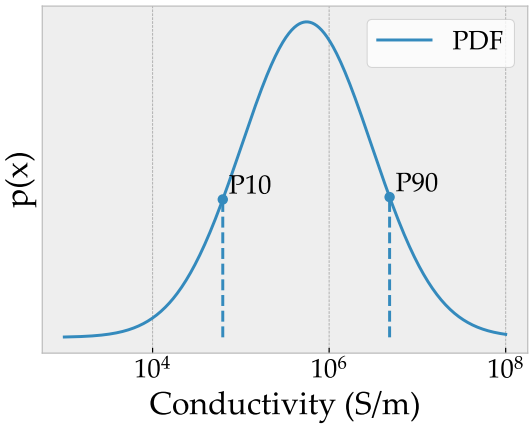

Figure E-3: Probability density function for the target's conductivity.

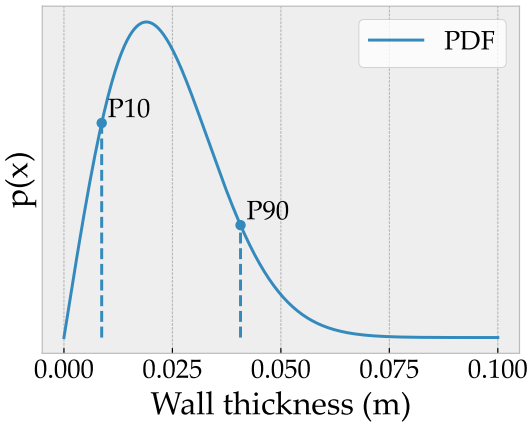

Figure E-4: Probability density function for the target's wall thickness.

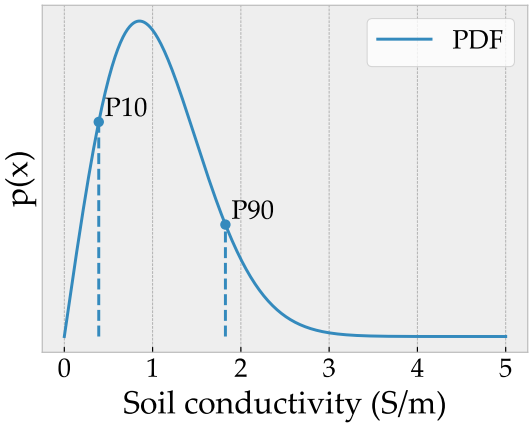

Figure E-5: Probability density function for the soil conductivity.